International Journal of Mechanical Sciences 241 (2023) 107963

Contents lists available at ScienceDirect

International Journal of Mechanical Sciences

journal homepage: www.elsevier.com/locate/ijmecsci

Comparative study on process-structure-property relationships of TiC/Ti6Al4V and Ti6Al4V by selective laser melting

Qinghong Jiang [a,b], Shuai Li [a], Sai Guo [a], Mingwang Fu [b,*], Bi Zhang [a,*]

[a] Shenzhen Key Laboratory of Cross-Scale Manufacturing Mechanics, Southern University of Science and Technology, Shenzhen 518055, China
[b] Department of Mechanical Engineering, Research Institute of Advanced Manufacturing, the Hong Kong Polytechnic University, Hung Hom, Kowloon, Hong Kong, China

ARTICLE INFO

Keywords:
Selective laser melting
Ti6Al4V titanium alloy
Titanium matrix composites
Process-structure-property relationship

ABSTRACT

Titanium matrix composites (TMCs) have gained tremendous attention due to their excellent mechanical properties by combining the advantages of Ti6Al4V matrix and ceramic reinforcement. In current study, the selective laser melting (SLM) technique is applied to manufacture TiC/Ti6Al4V and Ti6Al4V. Systematic characterization and analysis are conducted to reveal and compare their process-structure-property relationships. The results reveal that the near fully dense parts could be manufactured by process optimization upon the systematic investigation on their densification behaviors. The addition of TiC effectively refines the matrix grain and changes the microstructures. The SLM-manufactured (SLM-ed) Ti6Al4V exhibits typical coarse columnar grains with ultrafine lamellar α+β microstructures distributed inside (average α-lath thickness: 282 nm). Nevertheless, the SLM-ed TMCs possess a peculiar molten pool morphology, in which the sub-columnar grains grow upward along the direction of the steepest temperature gradient. The acicular nanoscale TiC is dispersed inside the sub-columnar grains, while the chain-like TiC is distributed along the boundary. Meanwhile, an evolution process is proposed to describe the microstructure evolution of the SLM-ed TMCs. The interrelationships between energy density and resulting microstructures are also identified, based on which, strong and ductile Ti6Al4V specimens (tensile strength: 1390 MPa, elongation: 9.66%) and ultra-strong TMCs specimens (tensile strength: 1538 MPa) are manufactured. The strengthening effects are mainly attributed to the Hall-Petch strengthening and load-bearing transformation. Fracture analysis indicates that the failure of the SLM-ed Ti6Al4V is caused by the micro-voids nucleation and coalescence at the interface of α and β phases, whereas the premature fracture of the SLM-ed TMCs is originated from the chain-like TiC.

1. Introduction

Ti6Al4V alloy has been widely utilized due to its high specific strength, excellent corrosion resistance, and good biocompatibility. However, the inferior tribological properties and high-temperature performance are the major concerns of the Ti6Al4V alloy in some critical applications [1]. The titanium matrix composites (TMCs), containing both hard reinforcement and Ti6Al4V matrix, exhibit improved wear resistance, high-temperature capability, as well as specific strength and stiffness. They have therefore been considered as a potential alternative material for aerospace, automotive, defense, and energy industries [2]. Additionally, among the typical reinforcement materials, TiC is known as an ideal candidate due to its good compatibility and comparable density with titanium alloy [3].

Conventional fabrication methods such as stir casting, squeeze casting, pray deposition, and powder metallurgy have been applied to fabricate TMCs parts [4,5]. However, these conventional methods present inevitable limitations, such as a long and complex manufacturing process, requiring specific molds for different parts, as well as high energy and time consumption. Recently, additive manufacturing has emerged and achieved a great progress in industries. Especially, SLM has been put into practice in many key applications due to its high technological maturity [6]. The SLM technique is not only capable of realizing rapid, integrated, and lightweight manufacturing of high-performance parts, but also is beneficial to obtaining refined microstructures because of the high cooling rate during an SLM process [7]. Meanwhile, the rapid solidification process can effectively suppress the material segregation and yield uniformly distributed reinforcements. As a result, SLM has been regarded as a promising method for the fabrication of TMCs, and therefore has attracted more research interests

* Corresponding authors.
E-mail addresses: ming.wang.fu@polyu.edu.hk (M. Fu), zhangb@sustech.edu.cn (B. Zhang).

https://doi.org/10.1016/j.ijmecsci.2022.107963
Received 17 July 2022; Received in revised form 10 October 2022; Accepted 19 November 2022
Available online 20 November 2022

in recent years [8].

However, SLM is a complex physical process, in which a concentrated laser beam with a high energy density scans and melts powder materials at a high speed. Accordingly, high temperature and stress gradient are induced in a local molten pool [9,10]. Meanwhile, convection, vaporization of the element with a low melting point, and the gradient surface tension lead to complex dynamic behaviors in the molten pool [11]. These phenomena could be exacerbated during the fabrication process of TMCs due to the extra interactions between the matrix and the reinforcement. Thus, defects such as pores, lack of fusion, and cracks are easily induced during the SLM process, resulting in a high porosity of the manufactured parts. Although near fully dense samples have been achieved in other TMCs such as SLM-ed TiB/Ti6Al4V, BN/Pure Ti [12,13], the SLM-ed TiC/Ti6Al4V with a high relative density is still rarely reported. Tang et al. [14] investigated the effects of process parameters on the fabrication quality of SLM-ed TiC/Ti6Al4V. According to their results, the highest relative density (RD) of the manufactured sample was 98.7%. The optimum RD of the SLM-ed TiC/Ti6Al4V achieved by Gu el al. [15] did not exceed 98.3%. Moreover, there is no established process database for the SLM fabrication of TiC/Ti6Al4V, and the process-structure-property relationships are also to be developed. Besides, the effects of TiC addition on the densification behavior, material structure, and performance are rarely reported.

To address the above issues, this study starts with an investigation on the process optimization to identify the process map and densification behaviors of the SLM-ed Ti6Al4V and TiC/Ti6Al4V. Subsequently, systematic characterizations are conducted to analyze the macro-defects and microstructure of samples manufactured by different process parameters. The tensile property and fracture mechanism of the SLM-ed Ti6Al4V and TiC/Ti6Al4V specimens are also compared. Finally, a comparative discussion is conducted to elucidate the process-structure-property relationships of the SLM-ed Ti6Al4V and TMCs.

2. Experimental preparation

2.1. Materials and SLM fabrication

The matrix material used in this study was spherical Ti6Al4V powders with a diameter size ranging from 15 to 45 μm. The reinforced material was irregular TiC powders with an average diameter of 500 nm. The volume fraction of TiC was selected as 5% since a good balance between printability and mechanical properties can be achieved [16]. The two kinds of powders were mixed in a swing mixer for 2 h with ceramic balls (ball-to-powder weight ratio was 1:3). As shown in Fig. 1d, the small TiC particles were uniformly attached and satellited on the surface of the Ti6Al4V powders.

The SLM fabrication was conducted in a commercial SLM machine (SLM®125HL, SLM Solutions, Germany), which was equipped with a 400 W fiber laser of a spot diameter of 64 μm. The SLM fabrication process was conducted in an argon atmosphere with an oxygen content less than 400 ppm, and the substrate was preheated and maintained at 200 °C to reduce temperature gradient. In the present study, cubic samples with a size of 8 × 8 × 8 mm were manufactured to determine the densification and process map. The parameter setting is summarized in Table 1; the hatch spacing and layer thickness were set at 80 μm and

Table 1
Processing parameters used to manufacture the cubic samples.

Process parameter	Value
Laser power P (W)	130 160 190 220 250
Scanning speed *v* (mm/s)	300 600 900 1200 1500
Hatch spacing *d* (μm)	80
Layer thickness *t* (μm)	30

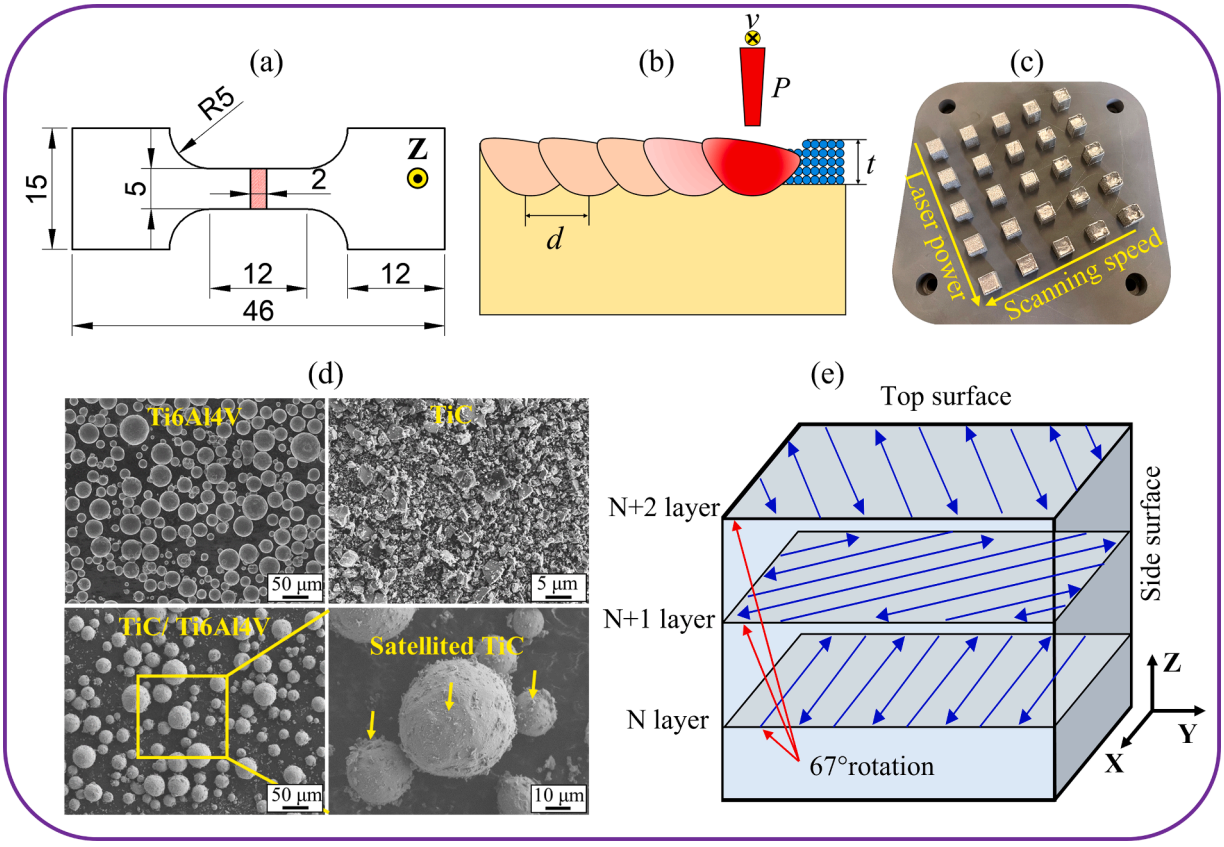

Fig. 1. (a) dimensional drawing of the tensile specimen (all dimensions are in mm); (b) schematic representation of the process parameters; (c) manufactured cubic samples; (d) SEM images of powder material; (e) schematic representation of the scanning strategy.

30 μm, respectively; and the laser power ranged from 130 to 250 W, while the scanning speed changed from 300 to 1500 mm/s. The volume energy density (E_d) was calculated by Eq. (1),

$$E_d = \frac{P}{vdt} \tag{1}$$

2.2. Material characterization

The SLM-ed cubic samples were cut from the substrate by wire-cutting and polished before further characterization. The Archimedes method was applied to measuring the RD. To determine the phase constitution, X-ray diffraction (XRD) was conducted with Cu Kα radiation at a scanning speed of 5 °/min (working voltage 45 kV, working current 200 mA). The etched samples (HF:HNO_3:H_2O=1:2.5:50) were detected by the optical microscopy (OM), while the microstructure analyses were also performed by the scanning electron microscopy (SEM) and the transmission electron microscopy (TEM). The grain characteristics and crystallographic orientation were further investigated by electron backscatter diffractometry (EBSD). Samples for EBSD were prepared by vibration polishing. The tensile test at room temperature was conducted on a universal testing machine equipped with a laser extensometer at a tensile speed of 0.5 mm/min. Fig. 1a shows the size and shape of tensile specimens and the specimens were manufactured to the final size by surface machining (Z direction refers to the building direction).

3. Results

3.1. Densification behavior

E_d is regarded as a crucial design parameter to control the fabrication quality of an SLM-ed part, thus the densification behavior at different E_d was systematically investigated by determining the densification maps and characterizing the cross-sectional morphology. Fig. 2a shows the densification map of the SLM-ed Ti6Al4V samples, which can be divided into three regions according to the densification levels. The samples manufactured in region I had an optimal densification level. Especially, the maximum RD (99.7%) was achieved when the applied E_d was around 65 J/mm^3. The high densification in region I was attributed to the low defect rate, and the defect-free cross-section morphology is shown in Fig. 2c and d. But small pores (≤50 μm) started to appear in region I with the increase of E_d (Fig. 2e). Region II was the window with a scanning speed of 600 mm/s, and the RD of samples in this region had a pronounced drop due to the introduction of a large number of medium pores (50–100 μm, Fig. 2f), which indicated that the scanning speed had significant effects on the RD of the SLM-ed parts. Moreover, large pores (≥100 μm, Fig. 2g) were introduced in region III in which the E_d exceeded 175 J/mm^3. Particularly, the samples manufactured in this region exhibited severe depression in the center area of the top surface due to the excessive heat input (Fig. 1c).

As presented in Fig. 2b, the SLM-ed TMCs showed a similar densification tendency. The RD first increased with an increasing E_d, then experienced a rapid decline. However, different densification behaviors were observed in the SLM-ed TMCs. The densification map of the SLM-ed TMCs was composed of four regions. Region I was the window with

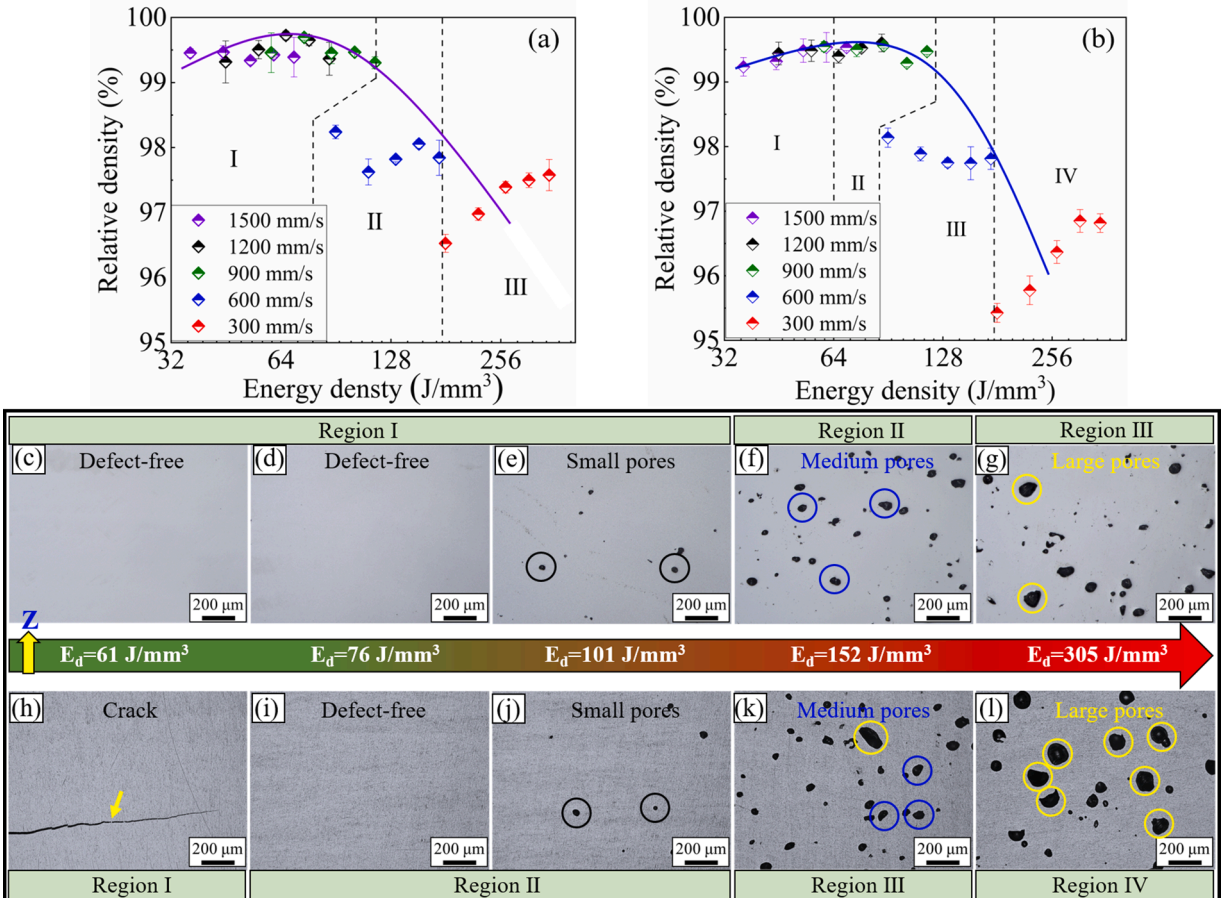

Fig. 2. Densification map: (a) SLM-ed Ti6Al4V; (b) SLM-ed 5%-TMCs. Optical images of cross sections after polishing: (c)–(g) SLM-ed Ti6Al4V; (h)-(l) SLM-ed TMCs. (small pore (black cycle): ≤50 μm; medium pores (blue cycle): 50–100 μm; large pores (yellow cycle): ≥100 μm).

an E_d lower than 65 J/mm^3, although the RD was also high, all the manufactured samples in this region were subjected to the interlayer cracking (Fig. 2h). With the increase of E_d, most samples in region II were crack-free (Fig. 2i) and remained a high RD, but the small pores were observed when E_d increased to 101 J/mm^3. Furthermore, more severe pore defects were observed in regions III and IV of the SLM-ed TMCs compared with that in the SLM-ed Ti6Al4V manufactured at the same E_d, which caused a sharper decline of the RD (Fig. 2k, l).

According to the fitting curves in Fig. 2a and b, when the applied E_d exceeded the optimum threshold, the RD decreased continuously with the increase of E_d due to the introduction of larger pores. However, a reverse tendency was observed when the E_d exceeded 180 J/mm^3 in both materials. In order to clarify the underling mechanism, the cross sections of these samples were also detected. As shown in Fig. 3, although the large pores were caused by the excessive energy, the subsurface layers nearby the top surface were pore-free in both materials. This is because severe surface bulge was accumulated under the enormous heat input as the increase of sample height, resulting in a failure of powder spreading. Thus the top surface was subjected to direct laser remelting, and the pores in the subsurface layers were effectively removed [17]. Moreover, the depth of the pore-free layers increased with the increase of laser power, which explained the upward tendency of the RD. However, the SLM-ed TMCs exhibited a relatively thinner pore-free layers compared with that of the SLM-ed Ti6Al4V.

3.2. Process map

Process maps and metallographic structures were combined to investigate the effects of process parameters on the manufacturing quality. As illustrated in Fig. 4a, the three regions in the densification map of the SLM-ed Ti6Al4V can also be projected on its process map. Especially, Region I was regarded as the optimum process window, in which all the manufactured samples exhibited a high RD, and a large proportion of this region can yield samples with an optimum RD higher than 99.5%. As shown in Fig. 4c and d, the metallographic structures of the samples manufactured in region I were typical prior β columnar grains. The boundaries of columnar grains were jagged and discontinuous because of the mismatch between successive layers induced by the 67° scan rotation strategy. Meanwhile, as the energy input increased, the width of the columnar grains increased due to a larger heat affected zone (Fig. 4e–g).

Fig. 4b displays the process map of the SLM-ed TMCs. Although the upper half part of the map shows a high RD, the SLM-ed TMCs had a narrower optimum process window compared to the SLM-ed Ti6Al4V due to the cracking effect in region I, which implied that the addition of TiC reversely affected the material printability. As shown in Fig. 4h–l, the metallographic structures of the SLM-ed TMCs exhibited a molten pool morphology instead of the columnar grains. When the lower energy input was applied ($\leq$ 65 J/mm^3), the molten pool exhibited a crescent shape with a small depth (Fig. 4h), resulting in an inferior bonding strength and finally cracking. As the E_d increased, semi-elliptical and regular molten pool morphologies were observed in Fig. 4i–j. A typical keyhole morphology with the pores distributed in the middle or bottom region was illustrated in Fig. 4k. Moreover, the samples manufactured with E_d up to 175 J/mm^3 were over-heated, and showed a large remelting depth.

3.3. Microstructure evolution

The representative 3D metallographic structures were assembled to further analyze the differences of metallographic structures between the SLM-ed Ti6Al4V and the TMCs. As shown in Fig. 5a, the side surfaces of the SLM-ed Ti6Al4V exhibited typical columnar prior β grains penetrating multiple layers due to the epitaxial growth [18]. While the top cross-section showed a rhombic-shaped grid morphology with the corner angle equal to 67°, and the side length of the rhombus was around 80 μm that was consistent with the hatching spacing, implying that the morphology was the direct reflection of the scanning strategy.

For the SLM-ed TMCs, the addition of TiC significantly changed the molten pool dynamics and the solidification behavior, thus resulting in a different microstructure. As displayed in Fig. 5b, the side surfaces of the SLM-ed TMCs possessed a molten pool morphology. Meanwhile, the intersecting molten pool paths with an included angle of 67 ° were observed in the top cross-section.

SEM images were taken to investigate the microstructural evolution in the SLM-ed TMCs. For the sample manufactured at a high E_d (305 J/mm^3), the molten pool showed a keyhole morphology (Fig. 6a). The TiC particles inside and outside the molten pool boundary (MPB) showed a distinct difference in feature size and morphology. The TiC particles inside the MPB were short rods with an average thickness of around 200 nm (Fig. 6b). While the TiC particles outside the MPB were long rods with the maximum thickness up to 595 nm due to the heat-treatment effect (Fig. 6c).

With a decrease in E_d, a higher cooling rate resulted in a more uniform and finer microstructure. As displayed in Fig. 6e, the TiC particles inside the MPB were nanoscale acicular. Although the TiC particles outside the MPB were slightly coarsened (Fig. 6f), the disparity of TiC size on both sides of the MPB showed a decline. Furthermore, in the sample prepared at a relatively low E_d, the chain-like eutectic TiC that symmetrically grew upward along the direction inclined to the center of the molten pool was detected (Fig. 6d).

XRD patterns of the SLM-ed Ti6Al4V and TMCs at different E_d are

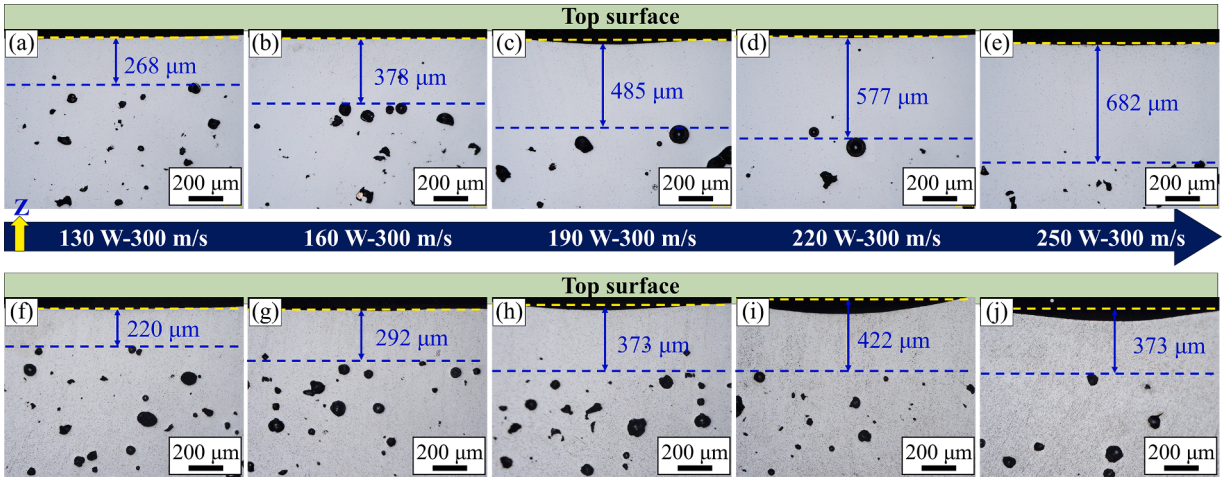

Fig. 3. Pore-free surface layer: (a)–(e) SLM-ed Ti6Al4V; (f)–(j) SLM-ed TMCs.

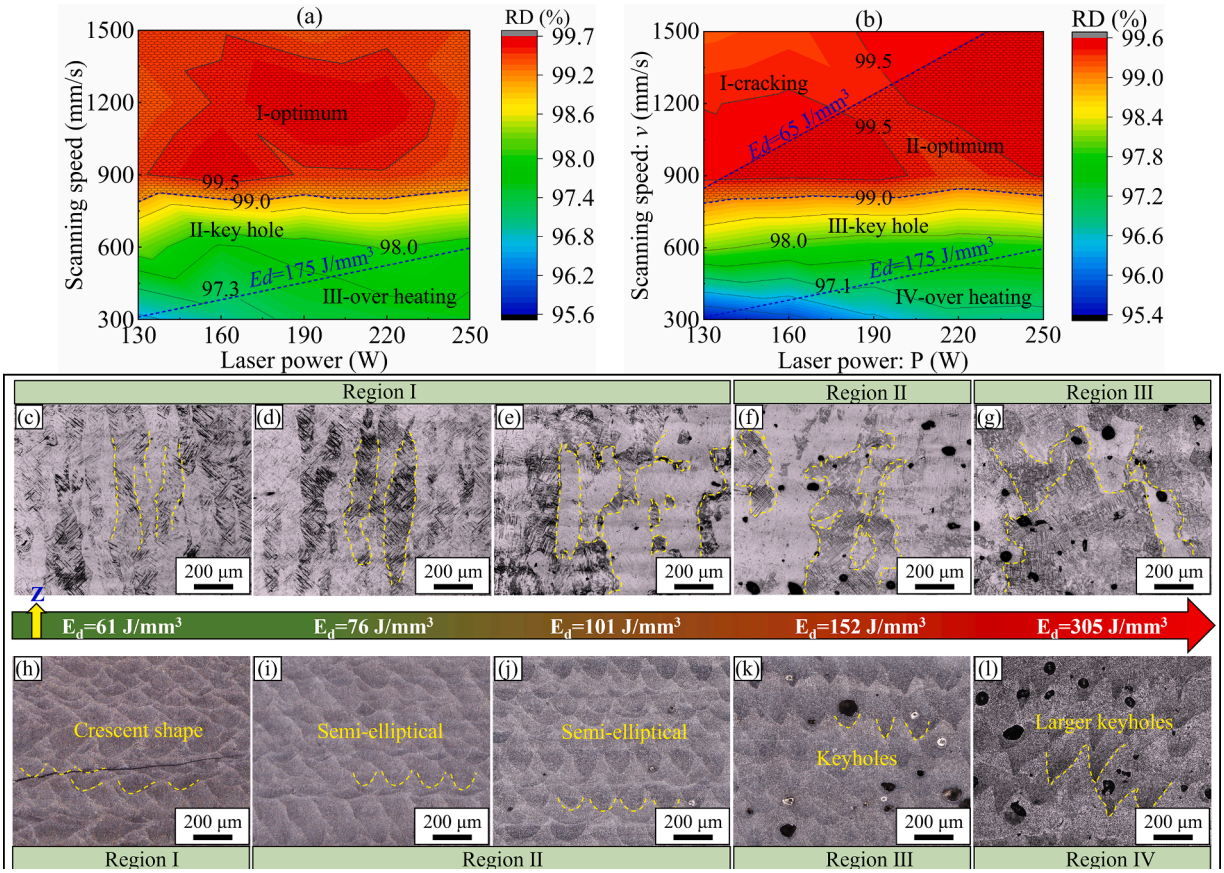

Fig. 4. Process map: (a) SLM-ed Ti6Al4V; (b) SLM-ed TMCs. Optical images of cross sections after etching: (c)–(g) SLM-ed Ti6Al4V; (h)-(l) SLM-ed TMCs.

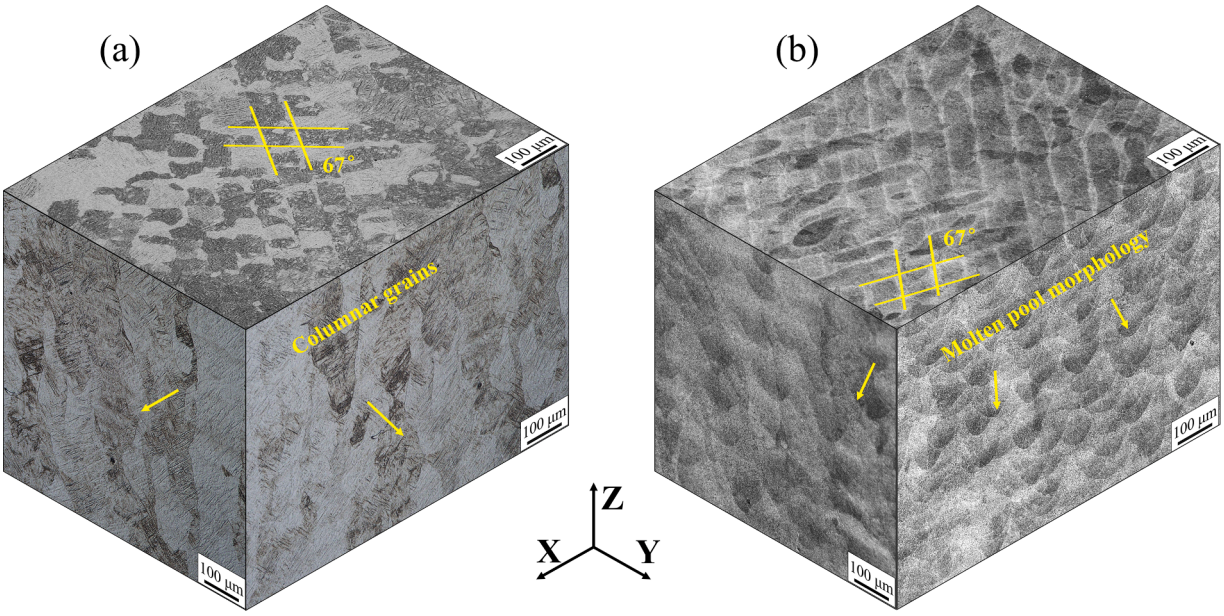

Fig. 5. Representative 3D metallographic structure (both samples were manufactured at 76 J/mm^3): Ti6Al4V, (b) TMCs.

shown in Fig. 7. The noticeable diffraction peaks of hexagonal close-packed (α'/α) Ti were identified at 2θ=35.4°, 38.6°, 40.5°, 53.3°, 63.9° in all the SLM-ed Ti6Al4V samples (Fig. 7a). Meanwhile, the diffraction peak of β-Ti was detected at 2θ=39.5° in the SLM-ed Ti6Al4V manufactured at E_d higher than 76 J/mm^3, which implied that the presence of a small amount of β phases. As the further decrease of E_d, the diffraction peak of β-Ti was absent. As a comparison, the related XRD diffraction profiles for the SLM-ed TMCs are presented in Fig. 7b, the diffraction peak of β phase was existed in all samples. For TiC reinforcement, the corresponding diffraction peaks were detected at 36.3°, 42.1°, 61.2°, respectively. Additionally, the peaks in these 2θ angles became weaker in intensity and been broadened with the decrease of E_d,

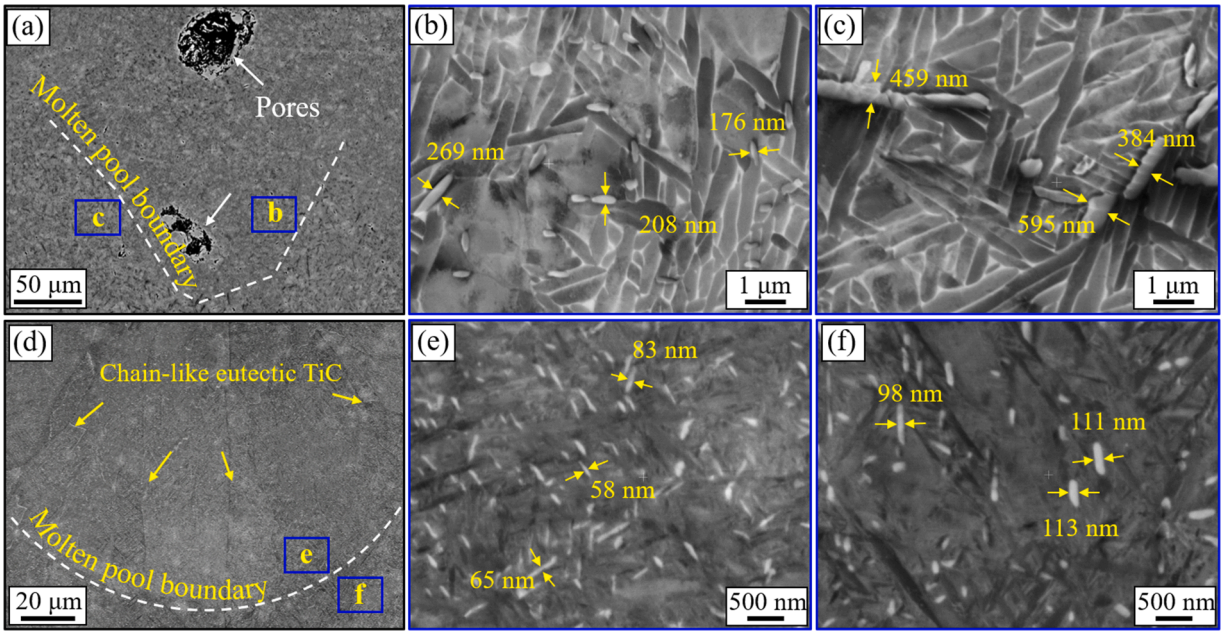

Fig. 6. SEM image of microstructure of SLM-ed TMCs from side surface: (a) 305 J/mm^3; (b) (c) enlarged view of box b and c in (a); (d) 76 J/mm^3; (e) (f) enlarged view of boxes b and c in (d).

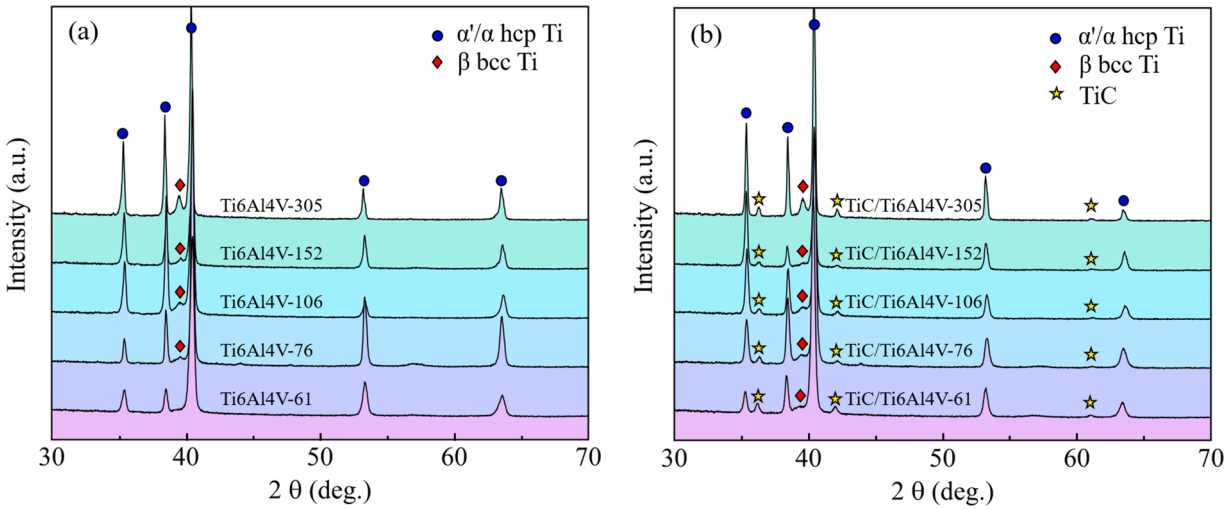

Fig. 7. XRD patterns of samples manufactured at different E_d: (a) SLM-ed Ti6Al4V; (b) SLM-ed TMCs.

implying the TiC particles were refined in the samples manufactured at a low E_d, this was further investigated in the following section.

Fig. 8 shows the SEM images (BSE mode) of the SLM-ed Ti6Al4V and TMCs manufactured at different E_d. The observed microstructures were in agreement with the results of the XRD detection. The lamellar α+β structures containing α-laths and retained β phases in between were obtained at high E_d (≥76 J/mm^3, Fig. 8a–d), while the fully martensitic α' microstructure was observed when the E_d was reduced to 61 J/mm^3 (Fig. 8e). Additionally, the grain size was significantly refined with the decrease of E_d. To quantitatively evaluate the grain refinement effect, the thickness of α'/α phase and TiC phase were counted by the Nano Measurer. As depicted in Fig. 9, the martensite thickness was reduced linearly from 537 nm in sample manufactured at E_d of 305 J/mm^3 to 201 nm in sample manufactured at E_d of 61 J/mm^3.

Since the microstructures inside and outside the MPB were not identical, the microstructures inside the molten pool of the SLM-ed TMCs were compared in Fig. 8f–j. Compared with the SLM-ed Ti6Al4V, the addition of TiC significantly refined the matrix material in the SLM-ed composites. For example, the martensite thickness was decreased by 31.5 % (257 nm to 176 nm) after the addition of TiC at the E_d of 76 J/mm^3. Meanwhile, both the matrix and reinforcement showed a similar refinement trend with the change of E_d. As shown in Fig. 8f, the coarse rod-shaped TiC with an average thickness of 202.4 nm was the dominant reinforcement in the sample manufactured at E_d of 305 J/mm^3. With the decline of E_d, the coarse TiC translated to nanoscale TiC with thickness less than 100 nm (Fig. 8g–j). For example, as the E_d decreased to 76 J/mm^3, the average thickness of TiC was down to 64 nm.

EBSD analyses were conducted on the samples manufactured at E_d of 76 J/mm^3 to further investigate the effects of TiC addition on grain and phase structures. As shown in the inverse pole figures (IPF) (Fig. 10a and d), the columnar prior β grain boundaries (marked with the black dashed lines) were discernible in both X-Y and X-Z views of the SLM-ed Ti6Al4V, which was in agreement with the metallographic observation. The lath shaped martensites confined within the columnar grains were regularly arranged, because the martensites phase developed from the parent β

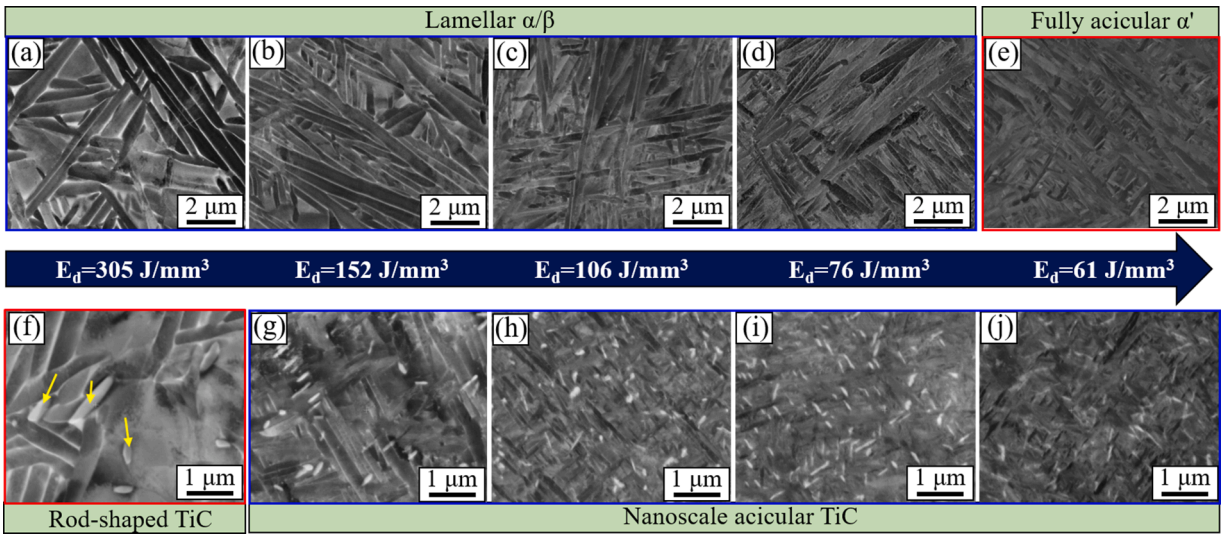

Fig. 8. SEM images of SLM-ed Ti6Al4V: (a) 305 J/mm^3; (b) 152 J/mm^3; (c) 101 J/mm^3; (d) 76 J/mm^3; (e) 61 J/mm^3. SEM images of SLM-ed TMCs: (f) 305 J/mm^3; (g) 152 J/mm^3; (h) 101 J/mm^3; (i) 76 J/mm^3; (j) 61 J/mm^3.

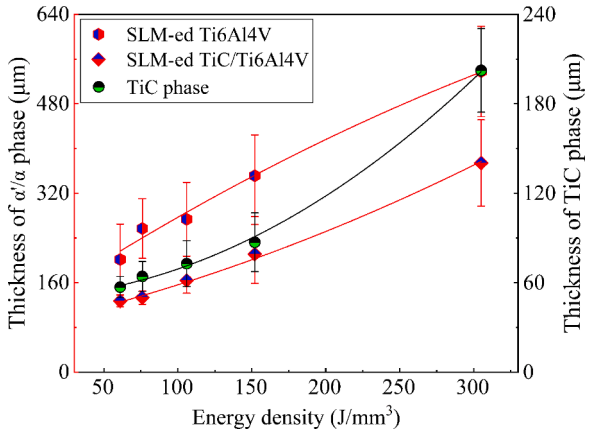

Fig. 9. Dependency of grain size of matrix and reinforcement on E_d.

phase follow the Burgers orientation relationship (BOR) ($\{0001\}_\alpha$//$\{110\}_\beta$, $<11\bar{2}0>_\alpha$//$<111>_\beta$) under the rapid cooling rate [19]. And different α martensite variants were staggered with each one shared a specific orientation (Fig. 10b and e). The phase maps are shown in Fig. 10c and f. The statistic results of the phase map show that the β phase accounted for 1.6 % and 1.9 % of the scanned area in the top and side surfaces, respectively. But the detected β phase showed a discontinuous state due to the limitation of resolution in EBSD [20].

For the SLM-ed TMCs, the molten pool boundaries were marked with the black dashed lines (Fig. 10g and j). Compared with the SLM-ed Ti6Al4V, the coarse columnar β grains were no longer present. Instead, the small β columnar grains were observed to grow symmetrically along the direction of the steepest temperature gradient, which was also consistent with the observation in Fig. 6d. Meanwhile, Fig. 10h and k show the high magnification EBSD images. The lamellar martensites were further limited in the chain-like TiC boundaries, the presence of the chain-like TiC phase (marked with white arrow) can be verified in the phase maps (Fig. 10i and l). However, only 3.2 % and 2.6 % of TiC were detected, which was lower than the theoretical value of 5%, this may be due to the EBSD resolution that limited the detection of the nanoscale TiC. Furthermore, the fraction of the β phase in the SLM-ed TMCs showed a slightly increase than that in the SLM-ed Ti6Al4V.

The grain boundary maps of the SLM-ed Ti6Al4V and the TMCs are shown in Fig. 11a and d (corresponding to the IPF image in Fig. 10b and Fig. 10h, respectively). Fig. 11b and e quantitatively compare the grain size (lamellar thickness of martensite) distribution. The grain size of the α phase in the SLM-ed Ti6Al4V ranged from 0 to 800 nm, and the average grain size was 282 nm. While the average grain size was refined to 175 nm after the addition of TiC. Fig. 11c and f show the misorientation angle distributions. The proportion of the low-angle grain boundary (LAGB: ≤15°) was 24.3% in the SLM-ed Ti6Al4V. It increased to 40.1% in the SLM-ed TMCs. Especially, the proportion of the sub-grain boundary (~2°-5°) exhibited a significant increase, which implied that the addition of TiC particles could effectively strengthen the grain boundary [21].

A high-resolution EBSD was collected to identify the orientation relationship (OR) between the TiC and α-Ti. As shown in Fig. 12b, the chain-like TiC grains were surrounded by α-Ti grains, taking the neighboring grains α-1, α-2, and α-3 as typical examples to analyze their OR with the TiC grains. The corresponding pole figures (PFs) are shown in Fig. 12c–f. It is clear that the α-1 grain share the OR of $\{0001\}_\alpha$// $\{111\}_{TiC}$, $<11\bar{2}0>_\alpha$//$<110>_{TiC}$ with TiC grain, which confirmed that the α-1 grain was nucleated on the TiC grain during the solidification process. While α-2 and α-3 grains had no OR related to the TiC grain, and the TiC grain served as a barrier to the growth of α grains in this scenario.

STEM/EDS analyses were employed to verify the microstructures and phase components in the SLM-ed Ti6Al4V and the TMCs. During the decomposition process, the Al element (α stabilizer) and V element (β stabilizer) are prone to segregate into the α and β phases, respectively, thus the retained β phase is V-rich but Al-deficient [22]. On this basis, the lamellar α+β microstructures containing α-laths and retained β phases can be verified in the HAADF images by combining the results of EDS mapping and line scanning. As shown in Fig. 13a and f, the lamellar α phase exhibits a finer size in the TMCs than that in the Ti6Al4V. Additionally, the presence of the nanoscale TiC can also be confirmed by the EDS mapping of the C element.

3.4. Tensile property and fracture mechanism

Fig. 14 exhibits the stress-strain curves of the Ti6Al4V and the TMCs manufactured under different process parameters. The corresponding yield strength, ultimate tensile strength (UTS), and elongation are summarized in Table 2. The SLM-ed Ti6Al4V-76 exhibited an outstanding mechanical property by combining UTS of 1390.52 MPa and elongation of 9.66%, which was much superior to that of the SLM-ed Ti6Al4V specimens in the previous studies. Meanwhile, the Ti6Al4V-101

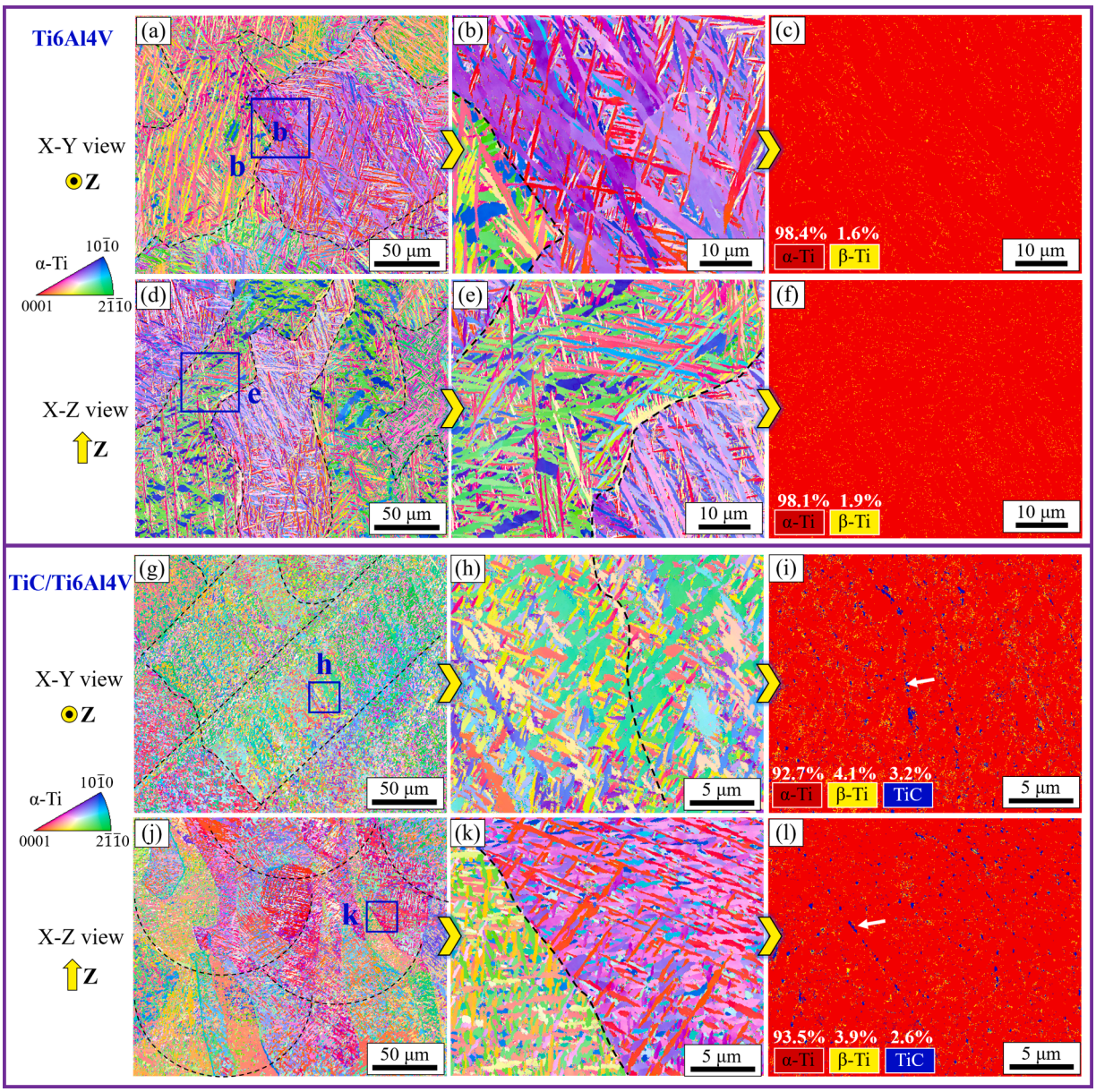

Fig. 10. EBSD analysis of SLM-ed Ti6Al4V. X-Y view: (a) IPF; (b) IPF of box b in (a); (c) phase map of (b). X-Z view: (d) IPF; (e) IPF of box e in (d); (f) phase map of (e). (g)–(l) are the corresponding EBSD analysis of SLM-ed TMCs.

also achieved excellent tensile properties (UTS: 1361.41 MPa, elongation: 7.62%), whereas the Ti6Al4V-152 showed an inferior tensile property (UTS: 1248.33 MPa, elongation: 5.46%) compared with Ti6Al4V-101 and Ti6Al4V-76.

As expected, the addition of TiC substantially enhanced the mechanical strength of the SLM-ed TMCs specimens. The UTS of the TMCs-152, 101, and 76 was 1365.83 MPa, 1424.16 MPa, and 1538.98 MPa, respectively, which was increased by 9.41%, 4.61%, 10.68% compared to that of the SLM-ed Ti6Al4V specimens manufactured under the same process parameters. However, the elongation of the TMCs specimens saw a large decline after the introduction of the hard and brittle TiC particles. Among the three sets of TMCs, the TMCs-76 achieved the highest elongation of 2.92%.

To investigate the underlying fracture mechanism, the fracture surfaces were analyzed. Fig. 15 displays the SEM fracture morphologies, and the insets are the corresponding macroscopic images after fracture. From the macroscopic morphologies, the fracture surfaces were oriented along with the direction of maximum shear stress in the SLM-ed Ti6Al4V specimens. Meanwhile, slight necking could be observed in the Ti6Al4V-152 and Ti6Al4V-101, while distinct necking appeared in the Ti6Al4V-76. As shown in Fig. 15a, noticeable pore defects surrounding with tearing ridges existed in the fracture surface of the Ti6Al4V-152, demonstrating that cracks tended to initiate and rapidly propagate from the pore defects during the loading process. Thus, the inferior mechanical strength of the Ti6Al4V-152 was highly related to its lower RD (98.05%). By contrast, pore defects were barely observed in the Ti6Al4V-101 and Ti6Al4V-76 due to their high RD (99.47%, 99.65%). The high magnification images revealed a dimple morphology in all the specimens, and the dimple size increased with an increasing plasticity in the Ti6Al4V-152 to Ti6Al4V-76.

However, the macro fracture surfaces of all SLM-ed TMCs specimens were perpendicular to the loading axis without a discernible necking effect due to their low ductility. The pore defects played an important role in the failure of the TMCs-152 (Fig. 15g), similar to what happened in the Ti6Al4V-152. The fracture morphologies of the SLM-ed TMCs showed a typical mixed fracture mode with tiny smooth cleavage planes

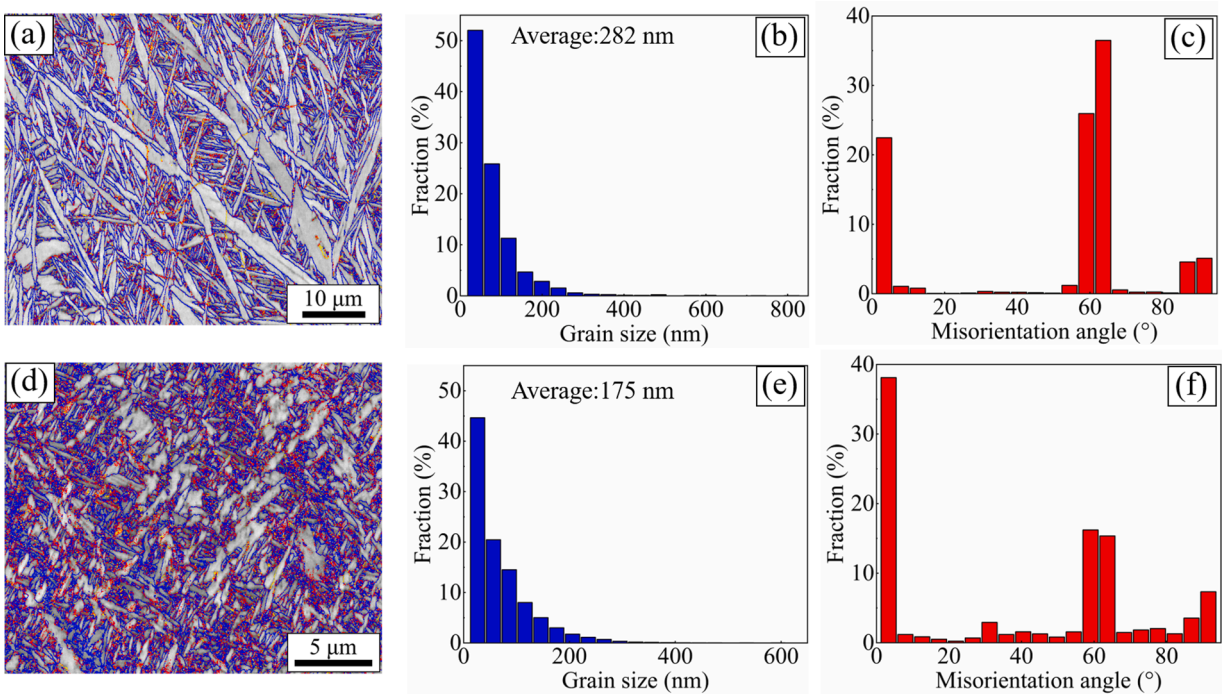

Fig. 11. Grain boundary maps: (a) Ti6Al4V; (d) TMCs. Grain size distribution: (b) Ti6Al4V; (e) TMCs. Misorientation angle distribution: (c) Ti6Al4V; (f) TMCs.

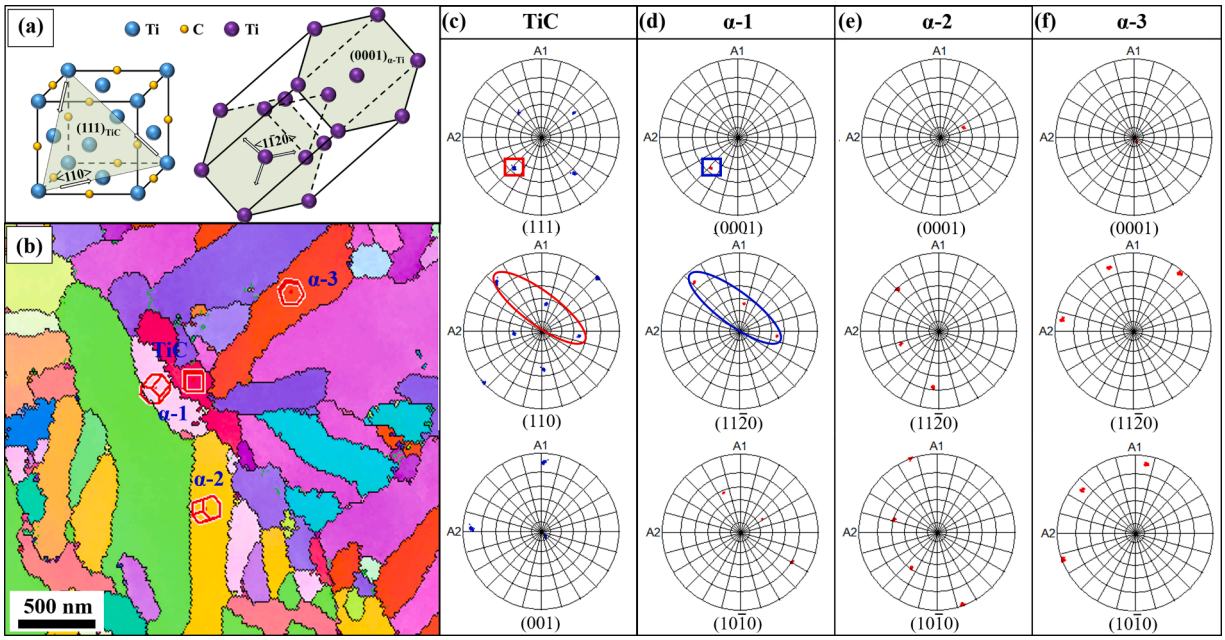

Fig. 12. (a) schematic representation of the orientation relationship between TiC and α-Ti; (b) high-resolution IPF of SLM-ed TMCs; (c)-(f) PFs of TiC and the α-Ti grains.

surrounding by small dimples and secondary cracks. As observed in the high magnification images (Fig. 15h, j, l), the fracture surfaces of the SLM-ed TMCs showed a dimple morphology with much smaller feature size than that in the SLM-ed Ti6Al4V.

To further investigate the deformation and damage evolution mechanisms, the longitudinal sections of the fracture surface were cut and observed. As displayed in Fig. 16a–c, the macroscopic fracture surfaces exhibited an increasing slant angle from Ti6Al4V-152 to Ti6Al4V-76. Fig. 16d–f display the microcracks closing to the fracture surface, most observed cracks propagated along with the direction of the maximum shear stress, except one crack shown in Fig. 16d that was aligned with the loading direction. In order to reveal the initiation of cracks, the longitudinal sections were etched and observed. As shown in Fig. 16g–i, under the external loading, the micro-voids tended to nucleate at the interface of the lamellar α and β aligning 45° with respect to the loading direction, and then coalesced along the α-laths, resulting in the initiation and propagation of cracks.

For the SLM-ed TMCs, small shear lips were observed in the longitudinal sections of the fracture surfaces (Fig. 17a–c). In the TMCs-152, cracks were found to propagate through the pore defects (Fig. 17d), this phenomenon was not observed in the Ti6Al4V counterpart, which implied that the SLM-ed TMCs had a higher sensitivity to pore defect

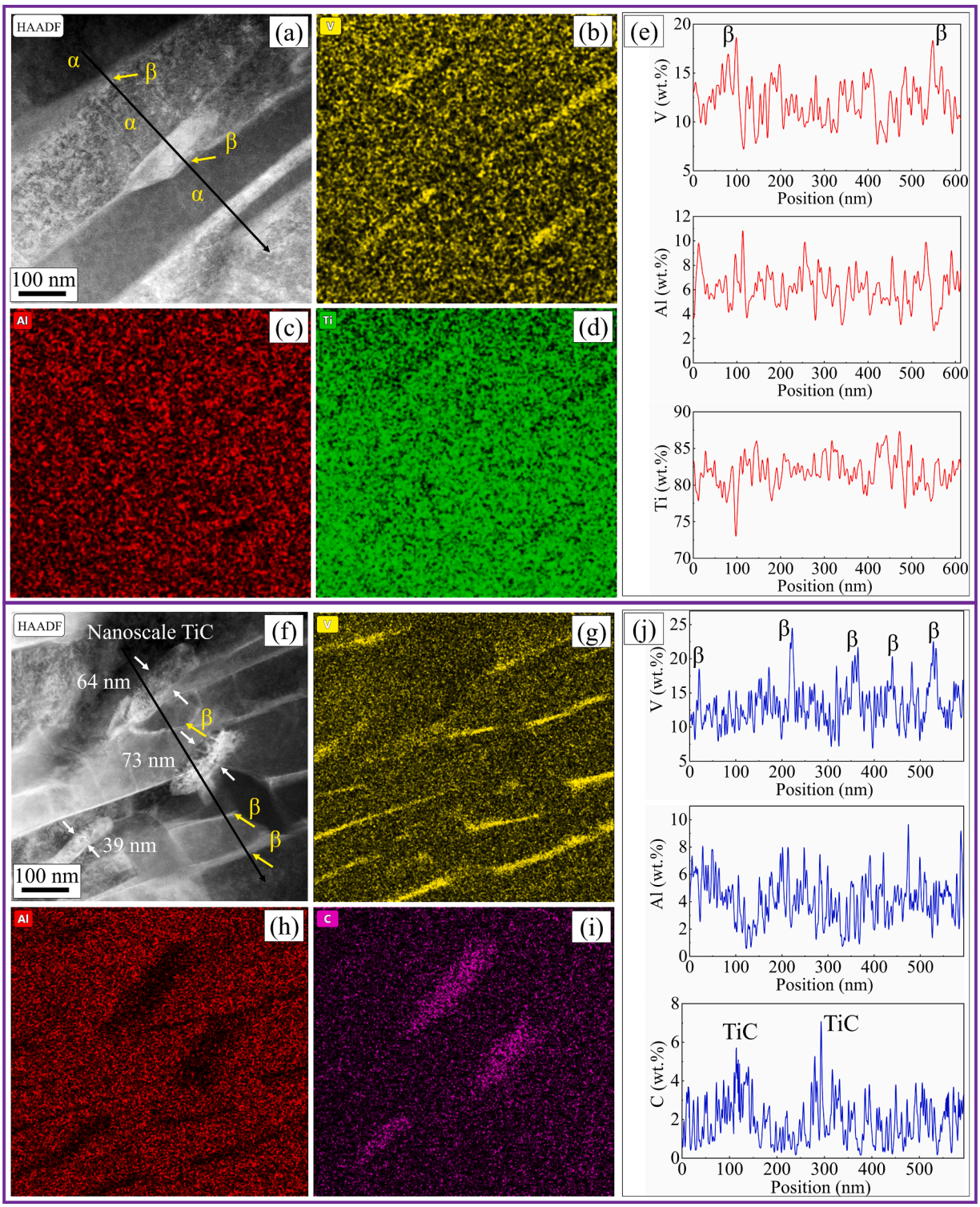

Fig. 13. HAADF images: (a) Ti6Al4V; (f) TMCs. EDS mapping: (b–d) Ti6Al4V; (g-i) TMCs. EDS line scanning along the black arrow: (e) Ti6Al4V; (j) TMCs.

during the fracture and failure process. Meanwhile, the pore-dominant fracture mechanism was inconspicuous with a decrease in porosity (Fig. 17e, f). In contrary to the SLM-ed Ti6Al4V, the chain-like eutectic TiC in the SLM-ed TMCs was the favorable propagation path for cracks according to the SEM images in Fig. 17g–i.

4. Discussion

Despite the successful applications of some SLM-ed alloy parts in industries, the property reliability and stability are difficult to control due to the high variability and low standardization during the SLM process, which poses enormous challenges to the qualification and certification of the SLM-ed parts [23]. Especially, for the SLM-ed TMCs, the addition of the reinforced particles significantly changes the dynamic behavior of the molten pool, macro-/micro-structures, as well as the final mechanical properties. Based on the results presented in the previous sections, a detailed discussion regarding the process-structure-property relationships of the SLM-ed Ti6Al4V and

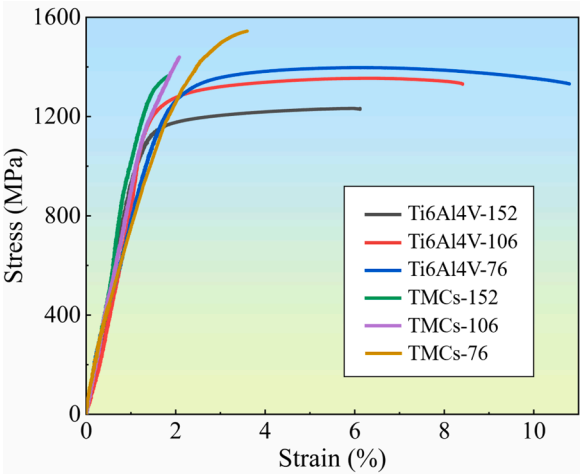

Fig. 14. Stress-strain curves of SLM-ed Ti6Al4V and TMCs.

Table 2
Results of tensile tests: $\sigma_{0.2}$-yield strength; σ_u-ultimate tensile strength; δ-elongation. (the suffix number in specimen name represents the applied E_d).

Specimen	$\sigma_{0.2}$ (MPa)	σ_u (MPa)	δ (%)
Ti6Al4V-152	1095.95 ± 10.34	1248.33 ± 13.88	5.46 ± 1.08
Ti6Al4V-101	1209.17 ± 7.26	1361.41 ± 6.67	7.62 ± 0.92
Ti6Al4V-76	1259.44 ± 13.63	1390.52 ± 17.74	9.66 ± 0.20
TMCs-152	1257.40 ± 6.55	1365.83 ± 7.98	1.27 ± 0.11
TMCs-101	1284.29 ± 9.97	1424.16 ± 14.77	1.47 ± 0.16
TMCs-76	1364.42 ± 16.86	1538.98 ± 22.23	2.92 ± 0.21

TMCs is conducted in this section.

4.1. Effect of process parameters on densification behavior

The SLM is a complex physical process involving numerous parameters. The defects would be easily induced if inappropriate parameters are applied, resulting in a considerable reduction of the mechanical properties of a manufactured part [24]. Thus, it is necessary to investigate the densification behavior to guide the parameter selection for industrial applications.

According to the results in Sections 3.1 and 3.2, although the RD of both materials shows a similar variation characteristic with the change of E_d, different densification behaviors are induced by the addition of 5% TiC particles. On the one hand, the presence of TiC with a higher melting point increases the energy requirement to achieve equal penetration depth and bonding strength. Accordingly, the higher energy is needed for the SLM-ed TMCs to avoid cracking, and the optimal E_d increases from 65 J/mm^3 in Ti6Al4V to 85 J/mm^3 in TMCs. On the other hand, when a relatively higher E_d is applied, the larger keyhole-induced pores are easily formed in the SLM-ed TMCs due to the higher local thermal input, resulting in a faster decline of the RD. Therefore, the addition of TiC particles increases the fabrication difficulty since the optimum process window of the SLM-ed TMCs is limited in a relatively narrower region.

With regard to the excessive energy input, the keyhole-induced porosities are produced and aggravated with the increasing E_d. At present, both *in-situ* monitoring experiments and high-fidelity simulations have been applied to investigate the pore formation mechanisms [25,26]. As shown in Fig. 18, the low-melting point elements evaporate easily when a laser beam with an excessive energy is applied, resulting in an exponential rise of the recoil pressure in a local zone (the recoil pressure P_{Recoil} can be calculated by Eq. (2). A keyhole-shaped depression zone is produced under the effect of the recoil pressure [25]. The keyhole traps a large number of rays due to the multiple reflections, and absorbs massive energy. This will lead to higher temperature and lower viscosity in the keyhole boundary, and keep the keyhole open at this moment. Meanwhile, a strong flow (as indicated by the green arrow) also exists under the influences of the recoil pressure and Marangoni effect. A protrusion zone is therefore introduced on top of the keyhole tail. As the laser beam moves forward, the protrusion zone collapses rapidly to the opposite [27]. As a result, the gas in the keyhole tail has no time to escape, and eventually, pores are formed as the melting material solidified along solidification front with most pores located at the bottom or middle of the molten pool.

Compared with the SLM-ed Ti6Al4V, the addition of TiC enhances the energy absorptivity due to the larger specific surface area and the higher laser absorptivity of finer TiC, which accumulates more heat in the local molten pool [28]. Accordingly, more metal evaporates and induces larger recoil pressure, finally leading to larger pores in the SLM-ed TMCs.

$$P_{Recodi} = 0.54\left[P_0 \exp\left(\frac{\Delta H_{lv}}{R \cdot T_{Boil}}\left(1 - \frac{T_{Boil}}{T}\right)\right)\right] \quad (2)$$

here,$P_0$is the ambient pressure; R is gas constant;$\Delta H_{lv}$is latent heat of evaporation material; and $T_{Boil}$is the boiling temperature.

4.2. Effect of process parameters on microstructure evolution

According to the results in Section 3.3, the SLM-ed TMCs possesses a distinct molten pool morphology, in which the sub-columnar grains grow upward along the direction of the steepest temperature gradient [29]. Meanwhile, the chain-like TiC grows along the boundary of sub-columnar grains, and the refined martensitic phase and nanoscale TiC distribute inside the sub-columnar grains. The formation of this unique microstructure is intimately connected to the complex melting-solidification process after the addition of TiC.

The reconstructed β-orientation maps are obtained by the MTEX toolbox to clarify the effect of TiC addition on the primary β grain. As shown in Fig. 19, the reconstructed β-orientation maps of SLM-ed Ti6Al4V and TMCs are corresponding to the EBSD results in Fig. 10d and j. The reconstructed β grains in SLM-ed Ti6Al4V are much thicker and penetrated multiple layers, which is matched with the observation of metallographic structures in Fig. 5. In contrast, the β grains are effectively refined and only a few grains are observed to extend between adjacent layers in the SLM-ed TMCs, which indicates the inhibiting effect of TiC addition on the growth of the columnar grains by the epitaxial growth.

As shown in Fig. 20, an evolution process is proposed to describe the microstructure formation during the fabrication process. The powders are melted when a high-energy laser beam is applied to the powder bed (Fig. 20a). All TiC particles are completely melted in this experiment since no unmelting TiC was observed in the manufactured samples. The 5% TMCs is in the hypoeutectic region according to the Ti-C binary phase diagram, the solidification process is determined by reactions (3)–(5) [30].

$$L \rightarrow \beta Ti + L_1 \quad (3)$$

$$L_1 \rightarrow \beta Ti + eutecticTiC \quad (4)$$

$$\beta Ti \rightarrow \alpha Ti \quad (5)$$

During the solidification process, the primary β grains are firstly solidified from the liquid phase along the molten pool boundary. When the temperature declines to the eutectic temperature (~1648 °C), the eutectic TiC and β-Ti would be formed through the eutectic reaction (reaction (4)). As shown in Fig. 20b, most eutectic reactions are carried out in the retained liquid phase between the primary β grains, during which the eutectic β-Ti and TiC nucleate and grow together. At the initiating state, the β-Ti phase nucleates and grows around the TiC

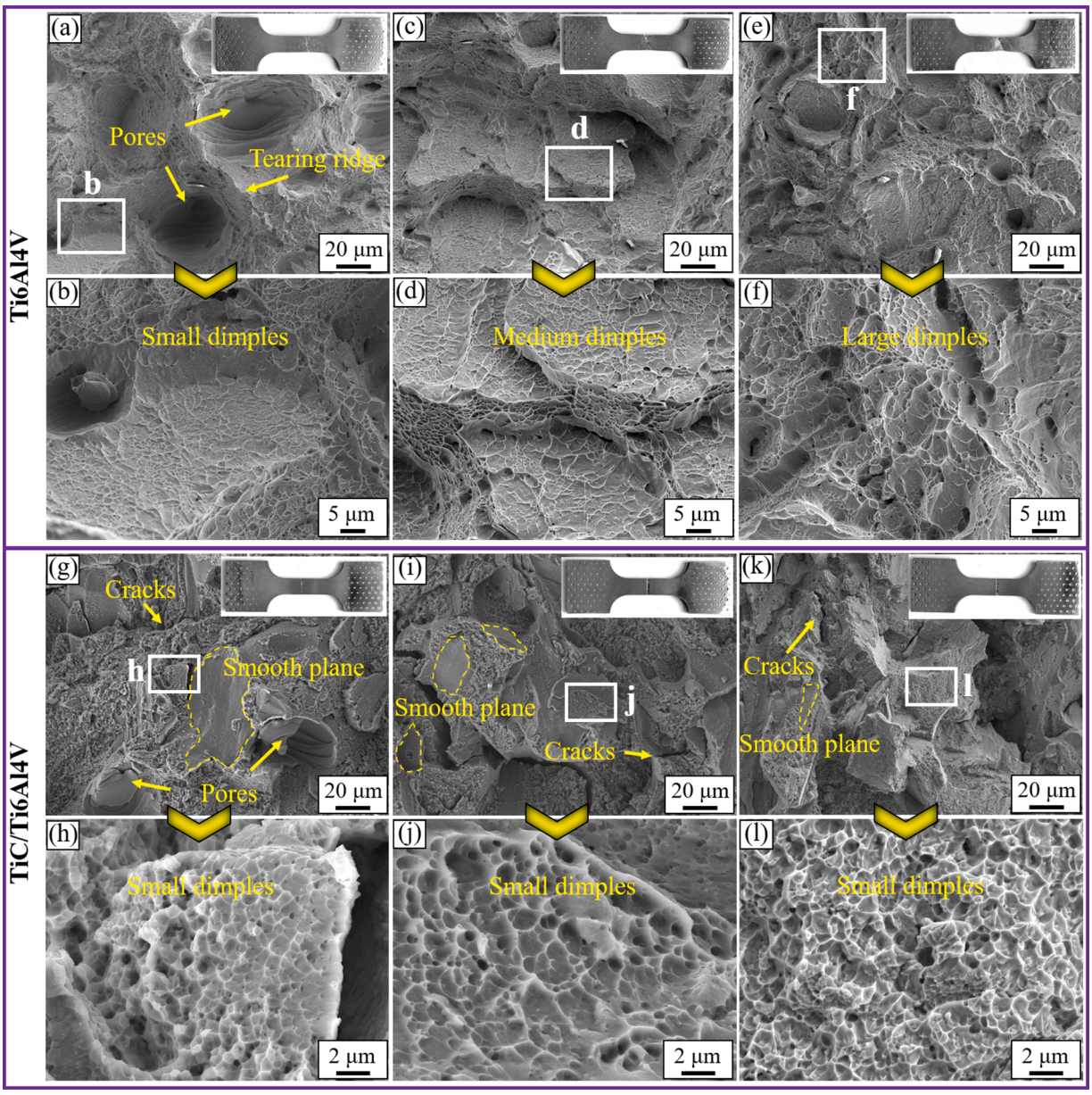

Fig. 15. SEM fracture morphologies of SLM-ed Ti6Al4V: (a), (b) Ti6Al4V-152; (c), (d) Ti6Al4V-101; (e), (f) Ti6Al4V-76. SEM fracture morphologies of SLM-ed TMCs: (g), (h) TMCs-152; (i), (j) TMCs-101; (k), (l) TMCs-76.

phase, and the most faces of TiC are surrounded by the β-Ti. Thus the TiC tends to grow along the direction contacting with the melt, forming the chain-like TiC in the boundary of the primary β grains [31]. Meanwhile, as the rapid solidification of β-Ti along the direction of the steepest temperature gradient, the TiC formed in the previous solidification front would be captured and trapped in the β-Ti grains (Fig. 20c).

As the temperature further decreases to the β-transition temperature, the α-Ti starts precipitating from the β-Ti by allotropic transformation (reaction (5)), and the retained β-Ti is distributed in between the α-Ti. During this process, the nano-scale TiC also serves as the nucleation site of α-Ti, and they share the OR of $\{0001\}_{\alpha}//\{111\}_{TiC}$, $<11\bar{2}0>_{\alpha}//<110>_{TiC}$, which was also confirmed in a previous study [3]. Meanwhile, according to a first-principles investigation [32], this OR is dedicated to strong interfacial fracture toughness and adhesion. In this scenario, the α-Ti nucleated on the TiC is no longer follow the BOR of with β-Ti. Nevertheless, for the α-Ti nucleated on β-Ti, the TiC restricts its growth by serving as a pinning barrier [12]. Additionally, SLM is a multilayer deposition process, the prior solidified materials are subjected to multiple thermal effects [33]. The resultant microstructures are schematically illustrated in Fig. 20f. The microstructures in the heat-affected zone are coarsened due to the *in-situ* "heat treatment".

Additionally, both the microstructures of the SLM-ed Ti6Al4V and TMCs are intimately tied to the E_d. For the SLM-ed Ti6Al4V, with a decrease in E_d, the microstructure changes from the lamellar α+β to the full α' microstructure (Fig. 8), while the thickness of the α phase shows a decline of 34.1% from the sample manufactured at E_d of 305 J/mm^3 to the sample manufactured at E_d of 61 J/mm^3 (Fig. 9). For the SLM-ed TMCs, both the matrix and reinforcement are obviously refined with the decrease of E_d. Furthermore, according to the EBSD results (Fig. 11), the average α phase grain size of the sample manufactured at E_d of 76 J/mm^3 is decreased from 282 nm in the SLM-ed Ti6Al4V to 175 nm in the SLM-ed TMCs, which implies that the induced TiC particles can significantly refine the Ti6Al4V matrix material. This is not only attributed to the higher nucleation rate, but also the higher cooling rate after the addition of TiC particles [12,34]. Additionally, the addition of TiC can significantly strengthen grain boundaries by promoting the formation of

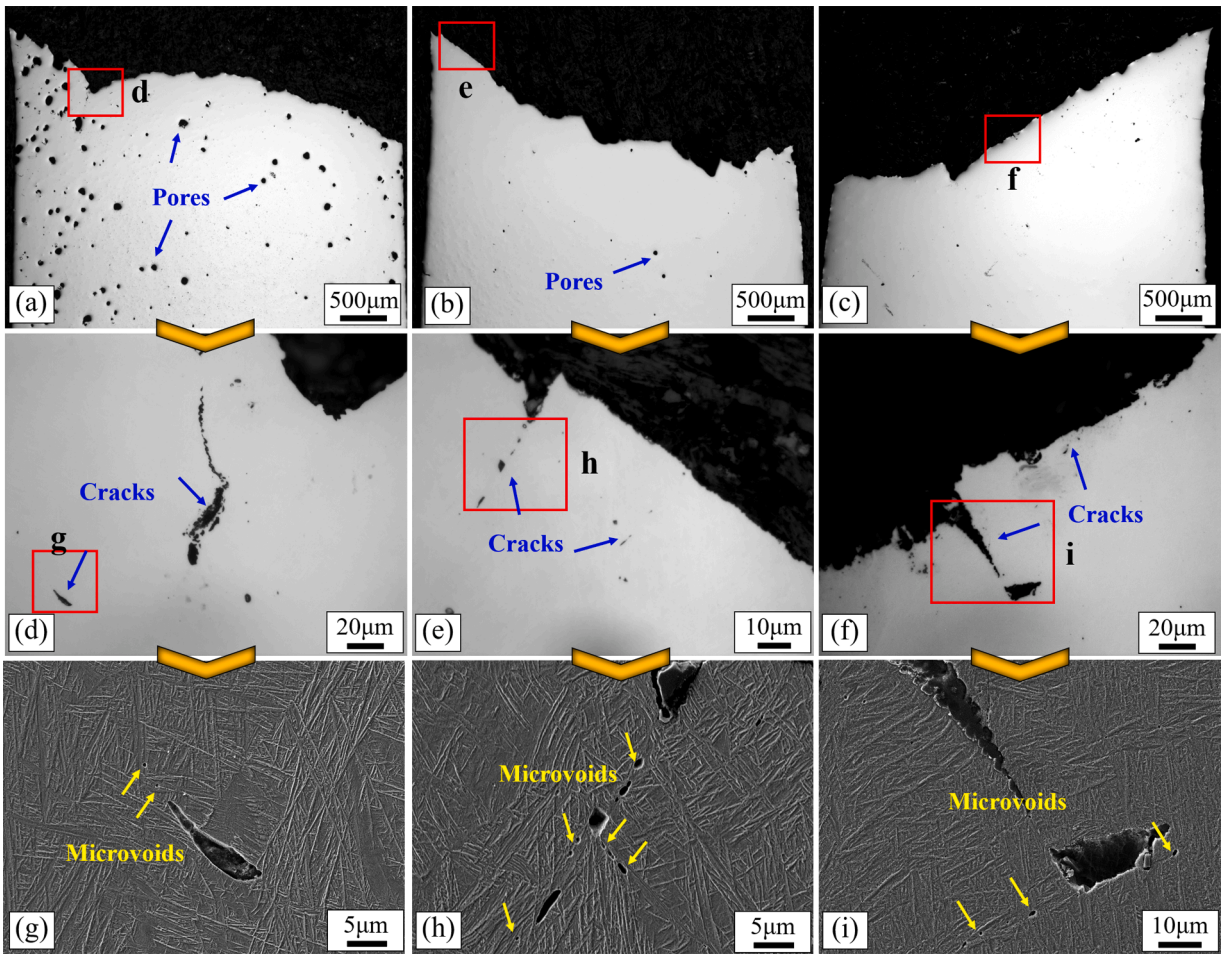

Fig. 16. Longitudinal sections of fracture surface: (a)–(c) Ti6Al4V-152 to Ti6Al4V-76; (g)–(i) enlarged views of d, e, f; (g)–(i) enlarged views of g, h, i (after etching).

more low-angle grains [21].

4.3. Strengthening mechanism

The TiC addition significantly improves the material strength due to direct and indirect strengthening [35,36]. The direct strengthening is mainly due to the load-bearing transformation. A strong bonding at the atomic level is induced at the interface between the dispersed nanoscale TiC and the matrix, resulting in a load-bearing strengthening. The strengthening stress of the load-bearing transformation can be evaluated by Eq. (6) [37]:

$$\Delta\sigma_{TiC} = 0.5\sigma_{0.2m}V_{TiC}(l/d)w_0 \tag{6}$$

where $\sigma_{0.2m}$ is yield stress of the Ti6Al4V matrix, V_{TiC}, l/d, w_0 are the volume fraction, aspect ratio, and orientation factor of the TiC reinforcement, respectively.

The indirect strengthening mainly attributes to the Hall-Petch strengthening. As shown in Fig. 9, the induced TiC particles effectively refined the matrix grains by promoting heterogeneous nucleation and constraining grain growth. A large number of new grain boundaries are induced by the grain refinement, which inhibits the dislocation motions among different grains and hence improves material strength [38]. The strengthening stress from the Hall-Petch strengthening can be evaluated by Eq. (7) [39]:

$$\Delta\sigma_{HP} = K\left(\frac{1}{\sqrt{d_2}} - \frac{1}{\sqrt{d_1}}\right) \tag{7}$$

where K is Hall-Petch constant, d_1 and d_2 refer to the average thickness of α phase in SLM-ed Ti6Al4V and TMCs.

According to the discussion above, the strengthening stresses result from the Hall-Petch strengthening and load-bearing transformation are quantitatively estimated. The applied parameters and calculation results are listed in Table 3. The calculated yield strength of TMCs-152 to TMCs-76 are 1230.46 MPa, 1340.87 MPa, and 1426.76 MPa, respectively, which approximately agree with the measured values. Specifically, the Hall-Petch strengthening is the dominant strengthening mechanism since it contributes 79%, 74%, and 75% of yield strength improvement in TMCs-152 to TMCs-76.

However, the material plasticity shows a significant decline after the addition of TiC, and the SLM-ed Ti6Al4V and TMCs also exhibit different deformation and failure mechanisms. For the SLM-ed Ti6Al4V, the local uncoordinated deformation at the interface of the α and β phases results in micro-voids nucleation and coalescence, leading to crack initiation and propagation, and finally material fracture. Nevertheless, the material fracture in the SLM-ed TMCs is originated from the chain-like TiC.

4.4. Correlation of process-structure-property

Process parameters govern the structures of a material, while the structures in turn determine the material properties. An understanding of the process-structure-property relationships is required to enable the fabrication of parts with tailored microstructures and desired properties for targeted applications. The essence of parameter controlling is to regulate energy input, a fully dense part can be manufactured by SLM under the appropriate energy density. The improved tensile properties are closely connected to the densification level, both tensile strength and elongation in the SLM-ed Ti6Al4V and the TMCs show a rapid decline

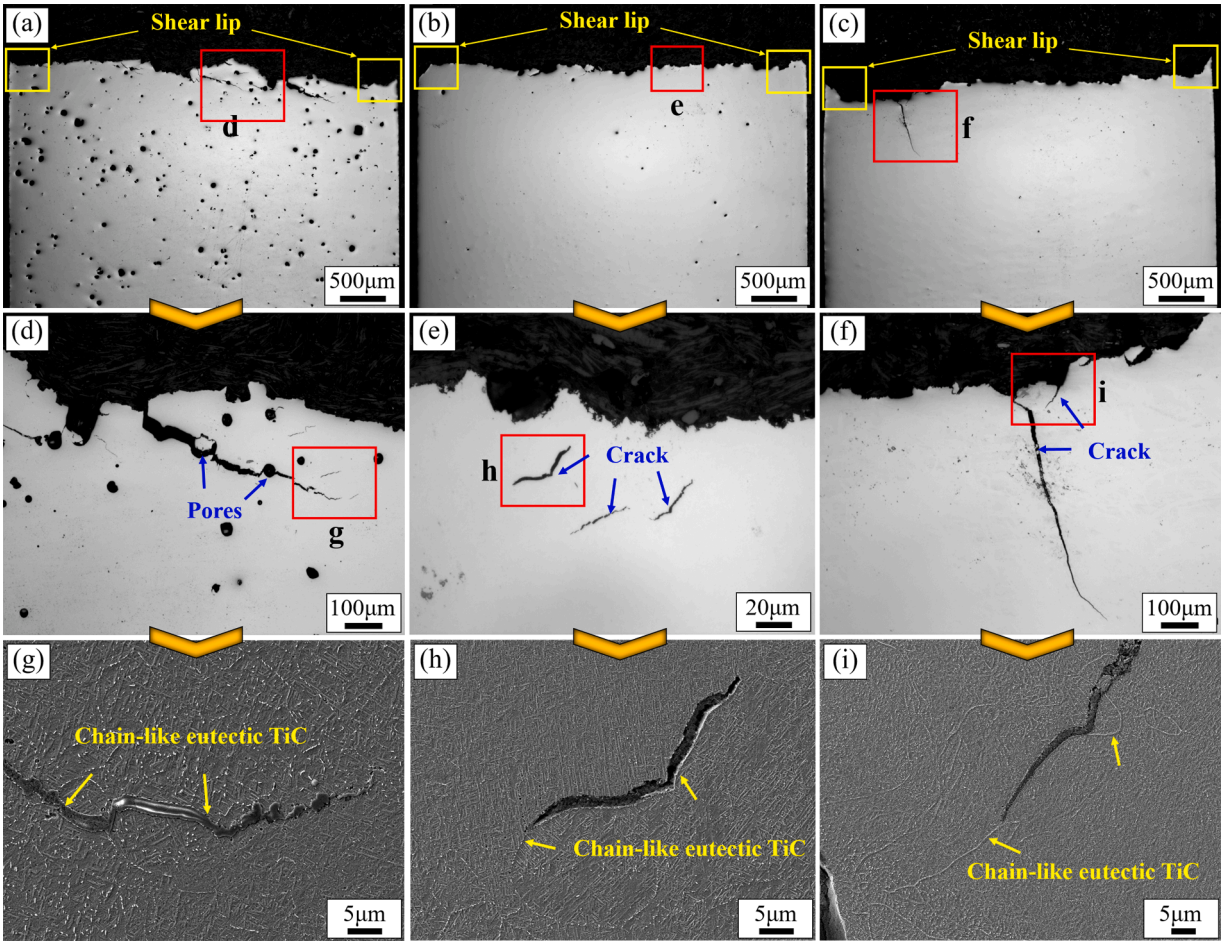

Fig. 17. Longitudinal sections of fracture surface: (a)-(c) TMCs-152 to TMCs-76; (g)-(i) enlarged views of d, e, f; (g)–(i) enlarged views of g, h, i (after etching).

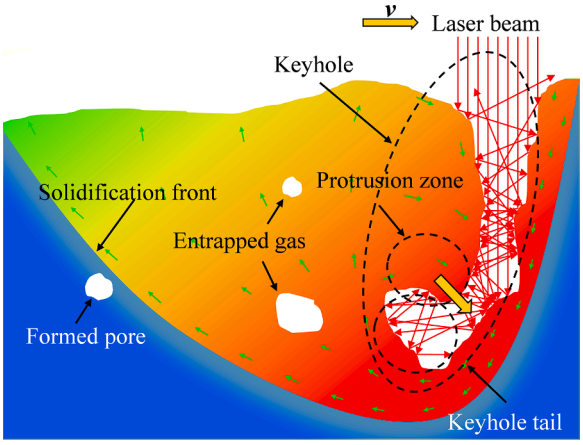

Fig. 18. Schematics of keyhole-induced pore formation process.

when defects are induced. This is because the defects can easily lead to crack nucleation and propagation under the external stress, especially for the SLM-ed TMCs which is more sensitive to pore defects due to the lower ductility.

On the other hand, the mechanical properties are also directly influenced by the microstructures. It was found that the yield strength of the SLM-ed Ti6Al4V and α-lath thickness had a relationship that was analogous to the Hall-Petch relationship [41]. Xu et al. [22,42] realized the *in-situ* α′ martensite decomposition by adjusting process parameters, the results indicated that the obtained ultrafine lamellar α+β microstructure could improve the strength and the ductility of SLM-ed Ti6Al4V simultaneously. Accordingly, the excellent tensile properties achieved in the SLM-ed Ti6Al4V-76 are also attributed to the ultrafine lamellar α+β microstructure with an average α-lath thickness of 282 nm.

Fig. 21 compares the tensile properties of the as-built specimens in this study and the as-built SLM-ed Ti6Al4V from recent references. From the previous studies, the as-built Ti6Al4V specimens by SLM usually exhibited a high tensile strength but low elongation (below 8%) due to the inherently brittle α′ martensite and the induced defects [43,44]. Consequently, the post-treatments with high costs such as heat treatment and hot isostatic pressing (HIP) are regarded as a necessary process to improve the material ductility, however, at the expense of strength reduction, falling into the so-called strength-ductility trade-off dilemma [45]. The SLM-ed Ti6Al4V specimens in this study show excellent tensile properties, particularly the Ti6Al4V-76, which achieves high tensile strength (1390 MPa) while maintaining high elongation (9.66%) simultaneously. Meanwhile, the SLM-ed TMCs specimens exhibit superior tensile strength with the highest tensile strength reaching 1538 MPa.

5. Conclusions

In this study, high-performance Ti6Al4V and TMCs are manufactured by the SLM technique. Systematic characterization and analysis are conducted to reveal and compare their process-structure-property relationships. The main findings are drawn as follows:

1 Densification maps and process maps facilitate the fabrication of near fully dense Ti6Al4V and TMCs samples by SLM. The addition of

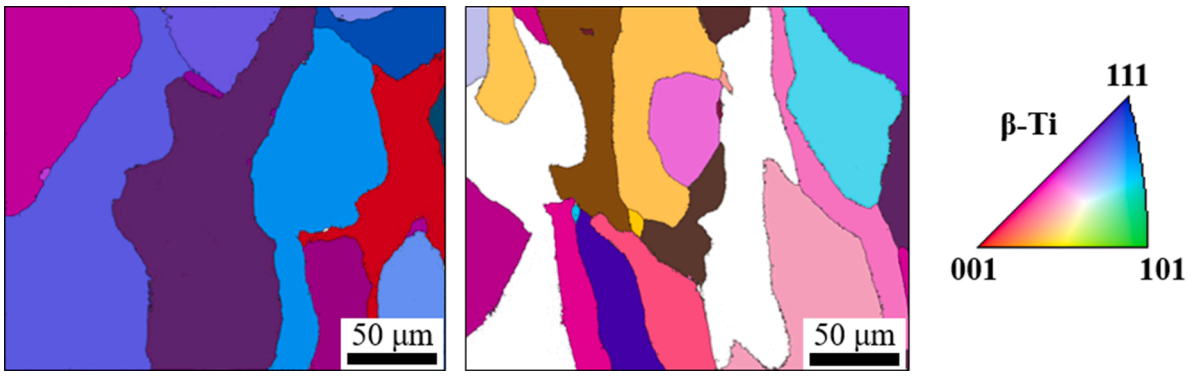

Fig. 19. Reconstructed β-orientation map: (a) Ti6Al4V; (b) TMCs.

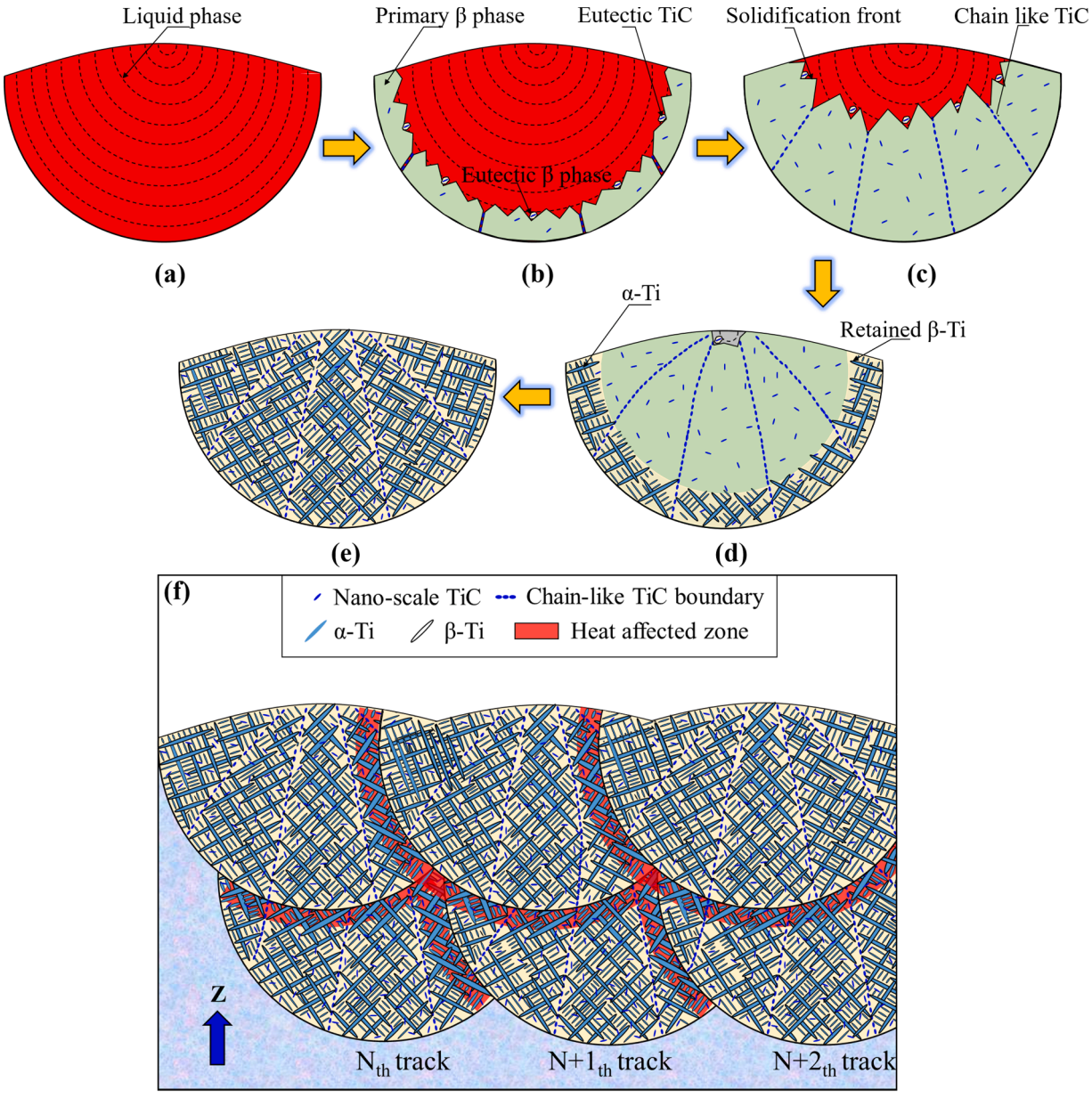

Fig. 20. Schematic illustration of the microstructural evolution of the SLM-ed TMCs: (a) melting process; (b) solidification of the primary β phase and eutectic reaction; (c) grain growth; (d) β→α transformation; (e) resultant microstructure in a molten pool; (e) final microstructure after multiple layer deposition.

Table 3
Calculation of strengthening stress (K=249.19 MPa/μm$^{1/2}$ [40], w_0=0.27 [12]).

Specimen	d_2 (μm)	d_1 (μm)	l/d	$\Delta\sigma_{HP}$ (MPa)	$\Delta\sigma_{TiC}$ (MPa)	Calculated $\sigma_{0.2}$ (MPa)	Measured $\sigma_{0.2}$ (MPa)
TMCs-152	0.224	0.351	3.81	106.32	28.18	1230.46	1257.40
TMCs-101	0.188	0.274	4.17	97.67	34.04	1340.87	1284.29
TMCs-76	0.176	0.282	5.01	124.73	42.59	1426.76	1364.42

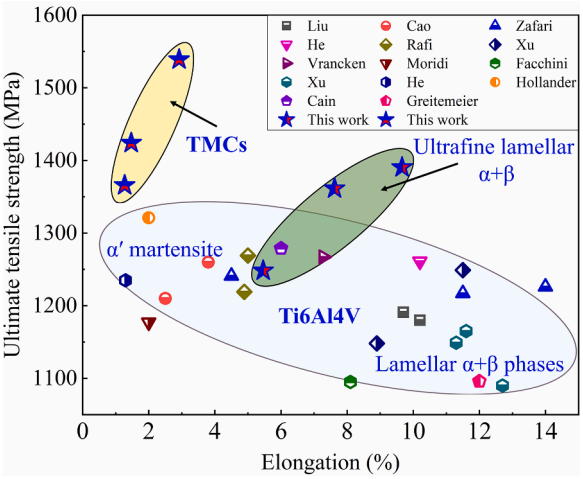

Fig. 21. Comparison of tensile properties of as-built SLM-ed specimens in this study and as-built SLM-ed Ti6Al4V from references [22,42,45–56].

the TiC particle increases the fabricating difficulty, a higher energy input is required for the SLM-ed TMCs to avoid interlayer cracking, resulting in a narrower optimum process window compared with that of SLM-ed Ti6Al4V.

2 The metallographic structure of the SLM-ed Ti6Al4V is the typical coarse columnar grain. An ultrafine lamellar α+β microstructure with an average α-lath thickness of 282 nm is obtained at the E_d of 76 J/mm^3. In contrast, the SLM-ed TMCs possess a distinct molten pool morphology. The grain size is further reduced to 175 nm after the addition of TiC by promoting heterogeneous nucleation and constraining grain growth, and the α-Ti grains nucleating on TiC follow the OR of $\{0001\}_\alpha//\{111\}_{TiC}$, $<11\bar{2}0>_\alpha//<110>_{TiC}$.

3 The Ti6Al4V specimens with the tensile strength of 1390 MPa and elongation of 9.66% are manufactured, which is mainly attributed to the high densification level and ultrafine microstructures. Meanwhile, the highest tensile strength of SLM-ed TMCs specimens reach 1538 MPa due to the load-bearing and Hall-Petch strengthening effects.

4 The SLM-ed Ti6Al4V and the TMCs have different deformation and failure mechanisms. Failure of the SLM-ed Ti6Al4V results from the micro-voids nucleation and coalescence at the interface of the lamellar α and β phases. However, for the SLM-ed TMCs, the chain-like TiC leads to the early crack initiation, propagation, and finally premature fracture.

CRediT authorship contribution statement

Qinghong Jiang: Conceptualization, Methodology, Investigation, Formal analysis, Writing – original draft. **Shuai Li:** Writing – review & editing. **Sai Guo:** Writing – review & editing. **Mingwang Fu:** Supervision, Writing – review & editing. **Bi Zhang:** Supervision, Funding acquisition, Writing – review & editing.

Declaration of Competing Interest

The authors declare that they have no known competing financial interests or personal relationships that could have appeared to influence the work reported in this paper.

Data availability

Data will be made available on request.

Acknowledgement

This work was supported by Shenzhen Science and Technology Innovation Commission for the project numbered JSGG20210420091802007, and the project of GRF No. 15228621, ZE1W and 1-CD4H from PolyU. The authors also wish to acknowledge the assistance from SUSTech Core Research Facilities.

Reference

[1] Huang X, Ding S, Yue W. Effect of cryogenic treatment on tribological behavior of Ti6Al4V alloy fabricated by selective laser melting. J Mater Res Technol 2021;12:1979–87. https://doi.org/10.1016/j.jmrt.2021.04.012.
[2] Hayat MD, Singh H, He Z, Cao P. Titanium metal matrix composites: an overview. Compos Part A 2019;121:418–38. https://doi.org/10.1016/j.compositesa.2019.04.005.
[3] Wang X, Li S, Han Y, Huang G, Mao J, Lu W. Visual assessment of special rod-like α-Ti precipitates within the *in situ* TiC crystals and the mechanical responses of titanium matrix composites. Compos Part B 2022;230:109511. https://doi.org/10.1016/j.compositesb.2021.109511.
[4] Yin S, Xie Y, Cizek J, Ekoi EJ, Hussain T, Dowling DP, Lupoi R. Advanced diamond-reinforced metal matrix composites via cold spray: properties and deposition mechanism. Compos Part B 2017;113:44–54. https://doi.org/10.1016/j.compositesb.2017.01.009.
[5] Ramanathan A, Krishnan PK, Muraliraja R. A review on the production of metal matrix composites through stir casting – furnace design, properties, challenges, and research opportunities. J Manuf Process 2019;42:213–45. https://doi.org/10.1016/j.jmapro.2019.04.017.
[6] Biffi CA, Fiocchi J, Bassani P, Tuissi A. Continuous wave vs pulsed wave laser emission in selective laser melting of AlSi10Mg parts with industrial optimized process parameters: microstructure and mechanical behavior. Addit Manuf 2018;24:639–46. https://doi.org/10.1016/j.addma.2018.10.021.
[7] Kim YK, Lee KA. Stabilized sub–grain and nano carbides–driven 1.2GPa grade ultra–strong CrMnFeCoNi high–entropy alloy additively manufactured by laser powder bed fusion. J Mater Sci Technol 2022;117:8–22. https://doi.org/10.1016/j.jmst.2021.12.010.
[8] Han C, Babicheva R, Chua JDQ, Ramamurty U, Tor SB, Sun CN, Zhou K. Microstructure and mechanical properties of (TiB+TiC)/Ti composites fabricated *in situ* via selective laser melting of Ti and B4C powders. Addit Manuf 2020;36:101466. https://doi.org/10.1016/j.addma.2020.101466.
[9] Lee KH, Yun GJ. A novel heat source model for analysis of melt pool evolution in selective laser melting process. Addit Manuf 2020;36:101497. https://doi.org/10.1016/j.addma.2020.101497.
[10] Fu J, Hu Z, Song X, Zhai W, Long Y, Li H, Fu M. Micro selective laser melting of NiTi shape memory alloy: defects, microstructures and thermal/mechanical properties. Opt Laser Technol 2020;131:106374. https://doi.org/10.1016/j.optlastec.2020.106374.
[11] Khairallah SA, Anderson AT, Rubenchik A, King WE. Laser powder-bed fusion additive manufacturing: physics of complex melt flow and formation mechanisms of pores, spatter, and denudation zones. Acta Mater 2016;108:36–45. https://doi.org/10.1016/j.actamat.2016.02.014.
[12] Zhou Z, Liu Y, Liu X, Zhan Q, Wang K. Microstructure evolution and mechanical properties of *in-situ* Ti6Al4V–TiB composites manufactured by selective laser melting. Compos Part B, 2021;207:108567. https://doi.org/10.1016/j.compositesb.2020.108567.
[13] Otte JA, Zou J, Dargusch MS. High strength and ductility of titanium matrix composites by nanoscale design in selective laser melting. J Mater Sci Technol 2022;118:114–27. https://doi.org/10.1016/j.jmst.2021.12.020.
[14] Tang M, Zhang L, Zhang N. Microstructural evolution, mechanical and tribological properties of TiC/Ti6Al4V composites with unique microstructure prepared by SLM. Mater Sci Eng A 2021;814:141187. https://doi.org/10.1016/j.msea.2021.141187.

[15] Gu D, Meng G, Li C, Meiners W, Poprawe R. Selective laser melting of TiC/Ti bulk nanocomposites: influence of nanoscale reinforcement. Scr Mater 2012;67(2): 185–8. https://doi.org/10.1016/j.scriptamat.2012.04.013.
[16] Wang J, Li L, Tan C, Liu H, Lin P. Microstructure and tensile properties of TiCp/Ti6Al4V titanium matrix composites manufactured by laser melting deposition. J Mater Process Technol 2018;252:524–36. https://doi.org/10.1016/j.jmatprotec.2017.10.005.
[17] Karimi J, Suryanarayana C, Okulov I, Prashanth KG. Selective laser melting of Ti6Al4V: effect of laser re-melting. Mater Sci Eng A 2021;805:140558. https://doi.org/10.1016/j.msea.2020.140558.
[18] Kumar P, Prakash O, Ramamurty U. Micro-and meso-structures and their influence on mechanical properties of selectively laser melted Ti-6Al-4V. Acta Mater 2018; 154:246–60. https://doi.org/10.1016/j.actamat.2018.05.044.
[19] Antonysamy A, Meyer J, Prangnell P. Effect of build geometry on the β-grain structure and texture in additive manufacture of Ti6Al4V by selective electron beam melting. Mater Charact 2013;84:153–68. https://doi.org/10.1016/j.matchar.2013.07.012.
[20] Wang X, Chou K. EBSD study of beam speed effects on Ti-6Al-4V alloy by powder bed electron beam additive manufacturing. J Alloy Compd 2018;748:236–44. https://doi.org/10.1016/j.jallcom.2018.03.173.
[21] Zhang L, Zhao Z, Bai P, Du W. EBSD investigation on microstructure evolution of *in-situ* synthesized TiC/Ti6Al4V composite coating. Mater Lett 2021;290:129449. https://doi.org/10.1016/j.matlet.2021.129449.
[22] Xu W, Lui EW, Pateras A, Qian M, Brandt M. *In situ* tailoring microstructure in additively manufactured Ti-6Al-4V for superior mechanical performance. Acta Mater 2017;125:390–400. https://doi.org/10.1016/j.actamat.2016.12.027.
[23] Seifi M, Salem A, Beuth J, Harrysson O, Lewandowski JJ. Overview of materials qualification needs for metal additive manufacturing. JOM 2016;68(3):747–64. https://doi.org/10.1007/s11837-015-1810-0.
[24] Zhou YH, Zhang ZH, Wang YP, Liu G, Zhou SY, Li YL, Shen J, Yan M. Selective laser melting of typical metallic materials: an effective process prediction model developed by energy absorption and consumption analysis. Addit Manuf 2019;25: 204–17. https://doi.org/10.1016/j.addma.2018.10.046.
[25] Zhao C, Parab ND, Li X, Fezzaa K, Tan W, Rollett AD, Sun T. Critical instability at moving keyhole tip generates porosity in laser melting. Science 2020;370(6520): 1080–6. https://doi.org/10.1126/science.abd1587.
[26] Khairallah SA, Martin AA, Lee JR, Guss G, Calta NP, Hammons JA, Nielsen MH, Chaput K, Schwalbach E, Shah MN. Controlling interdependent meso-nanosecond dynamics and defect generation in metal 3D printing. Science 2020;368(6491): 660–5. https://doi.org/10.1126/science.aay7830.
[27] Bayat M, Thanki A, Mohanty S, Witvrouw A, Yang S, Thorborg J, Tiedje NS, Hattel JH. Keyhole-induced porosities in laser-based powder bed fusion (L-PBF) of Ti6Al4V: high-fidelity modelling and experimental validation. Addit Manuf 2019; 30:100835. https://doi.org/10.1016/j.addma.2019.100835.
[28] Ge Q, Gu D, Dai D, Ma C, Sun Y, Shi X, Li Y, Zhang H, Chen H. Mechanisms of laser energy absorption and melting behavior during selective laser melting of titanium-matrix composite: role of ceramic addition. J Phys D Appl Phys 2021;54(11): 115103. https://doi.org/10.1088/1361-6463/abcdce.
[29] Fereiduni E, Ghasemi A, Elbestawi M. Unique opportunities for microstructure engineering via trace B4C addition to Ti-6Al-4V through laser powder bed fusion process: as-built and heat-treated scenarios. Addit Manuf 2022;50:102557. https://doi.org/10.1016/j.addma.2021.102557.
[30] Ya B, Zhou B, Yang H, Huang B, Jia F, Zhang X. Microstructure and mechanical properties of *in situ* casting TiC/Ti6Al4V composites through adding multi-walled carbon nanotubes. J Alloy Compd 2015;637:456–60. https://doi.org/10.1016/j.jallcom.2015.03.044.
[31] Wang J, Li L, Lin P, Wang J. Effect of TiC particle size on the microstructure and tensile properties of TiCp/Ti6Al4V composites fabricated by laser melting deposition. Opt Laser Technol 2018;105:195–206. https://doi.org/10.1016/j.optlastec.2018.03.009.
[32] Li J, Yang Y, Feng G, Luo X, Sun Q, Jin N. Adhesion and fracture toughness at α-Ti (0001)/TiC(111): a first-principles investigation. Appl Surf Sci 2013;286:240–8. https://doi.org/10.1016/j.apsusc.2013.09.058.
[33] Jing G, Huang W, Yang H, Wang Z. Microstructural evolution and mechanical properties of 300 M steel produced by low and high power selective laser melting. J Mater Sci Technol 2020;47(13):44–56. https://doi.org/10.1016/j.jmst.2019.12.020.
[34] Cai C, Radoslaw C, Zhang J, Yan Q, Wen S, Song B, Shi Y. *In-situ* preparation and formation of TiB/Ti-6Al-4V nanocomposite via laser additive manufacturing: Microstructure evolution and tribological behavior. Powder Technol 2019;342. https://doi.org/10.1016/j.powtec.2018.09.088.
[35] Yu WH, Sing SL, Chua CK, Kuo CN, Tian XL. Particle-reinforced metal matrix nanocomposites fabricated by selective laser melting: a state of the art review. Prog Mater Sci 2019;104:330–79. https://doi.org/10.1016/j.pmatsci.2019.04.006.
[36] Sanaty-Zadeh A, Rohatgi PK. Comparison between current models for the strength of particulate-reinforced metal matrix nanocomposites with emphasis on consideration of Hall–Petch effect. Mater Sci Eng A 2012;531:112–8. https://doi.org/10.1016/j.msea.2012.04.039.
[37] Hu Y, Cong W, Wang X, Li Y, Ning F, Wang H. Laser deposition-additive manufacturing of TiB-Ti composites with novel three-dimensional quasi-continuous network microstructure: effects on strengthening and toughening. Compos Part B 2018;133:91–100. https://doi.org/10.1016/j.compositesb.2017.09.019.
[38] Jiang Q, Li S, Zhou C, Zhang B, Zhang Y. Effects of laser shock peening on the ultra-high cycle fatigue performance of additively manufactured Ti6Al4V alloy. Opt Laser Technol 2021;144:107391. https://doi.org/10.1016/j.optlastec.2021.107391.
[39] AlMangour B, Kim YK, Grzesiak D, Lee KA. Novel TiB2-reinforced 316L stainless steel nanocomposites with excellent room- and high-temperature yield strength developed by additive manufacturing. Compos Part B 2019;156:51–63. https://doi.org/10.1016/j.compositesb.2018.07.050.
[40] Ren Y, Zhou SM, Xue ZY, Luo WB, Ren YJ, Zhang YJ. Effect of α-platelet thickness on the mechanical properties of Ti-6Al-4V alloy with lamellar microstructure. IOP Conf Ser Mater Sci Eng 2017;281:012024. https://doi.org/10.1088/1757-899X/281/1/012024.
[41] Xu W, Brandt M, Sun S, Elambasseril J, Liu Q, Latham K, Xia K, Qian M. Additive manufacturing of strong and ductile Ti–6Al–4V by selective laser melting via *in situ* martensite decomposition. Acta Mater 2015;85:74–84. https://doi.org/10.1016/j.actamat.2014.11.028.
[42] Xu W, Sun S, Elambasseril J, Liu Q, Brandt M, Qian M. Ti-6Al-4V additively manufactured by selective laser melting with superior mechanical properties. JOM 2015;67(3):668–73. https://doi.org/10.1007/s11837-015-1297-8.
[43] Zhang B, Li Y, Bai Q. Defect formation mechanisms in selective laser melting: a review. Chin J Mech Eng 2017;30(3):515–27. https://doi.org/10.1007/s10033-017-0121-5.
[44] Singla AK, Banerjee M, Sharma A, Singh J, Bansal A, Gupta MK, Khanna N, Shahi AS, Goyal DK. Selective laser melting of Ti6Al4V alloy: process parameters, defects and post-treatments. J Manuf Process 2021;64:161–87. https://doi.org/10.1016/j.jmapro.2021.01.009.
[45] Liu J, Sun Q, Zhou CA, Wang X, Li H, Guo K, Sun J. Achieving Ti6Al4V alloys with both high strength and ductility via selective laser melting. Mater Sci Eng A 2019; 766:138319. https://doi.org/10.1016/j.msea.2019.138319.
[46] Cain V, Thijs L, Humbeeck JV, Hooreweder BV. Crack propagation and fracture toughness of Ti6Al4V alloy produced by selective laser melting. Addit Manuf 2015; 5:68–76. https://doi.org/10.1016/j.addma.2014.12.006.
[47] He J, Li D, Jiang W, Ke L, Qin G, Ye Y, Qin Q, Qiu D. The martensitic transformation and mechanical properties of Ti6Al4V prepared via selective laser melting. Materials 2019;12(2):321. https://doi.org/10.3390/ma12020321.
[48] Facchini L, Magalini E, Robotti P, Molinari A, Höges S, Wissenbach K. Ductility of a Ti-6Al-4V alloy produced by selective laser melting of prealloyed powders. Rapid Prototyp J 2010;16(6):450–9. https://doi.org/10.1108/13552541011083371.
[49] Vrancken B, Thijs L, Kruth JP, Humbeeck JV. Heat treatment of Ti6Al4V produced by selective laser melting: microstructure and mechanical properties. J Alloy Compd 2012;541:177–85. https://doi.org/10.1016/j.jallcom.2012.07.022.
[50] He B, Wu W, Zhang L, Lu L, Yang Q, Long Q, Kun C. Microstructural characteristic and mechanical property of Ti6Al4V alloy fabricated by selective laser melting. Vacuum 2018;150:79–83. https://doi.org/10.1016/j.vacuum.2018.01.026.
[51] Greitemeier D, Dalle Donne C, Syassen F, Eufinger J, Melz T. Effect of surface roughness on fatigue performance of additive manufactured Ti–6Al–4V. Mater Sci Technol 2016;32(7):629–34. https://doi.org/10.1179/1743284715Y.0000000053.
[52] Hollander DA, Walter MV, Wirtz T, Sellei R, Schmidt-Rohlfing B, Paar O, Erli HJ. Structural, mechanical and *in vitro* characterization of individually structured Ti-6Al-4V produced by direct laser forming. Biomaterials 2006;27(7):955–63. https://doi.org/10.1016/j.biomaterials.2005.07.041.
[53] Moridi A, Demir AG, Caprio L, Hart AJ, Previtali B, Colosimo BM. Deformation and failure mechanisms of Ti–6Al–4V as built by selective laser melting. Mater Sci Eng A, 2019;768:138456. https://doi.org/10.1016/j.msea.2019.138456.
[54] Rafi HK, Karthik NV, Gong H, Starr TL, Stucker BE. Microstructures and mechanical properties of Ti6Al4V parts fabricated by selective laser melting and electron beam melting. J Mater Eng Perform 2013;22(12):3872–83. https://doi.org/10.1007/s11665-013-0658-0.
[55] Zafari A, Barati MR, Xia K. Controlling martensitic decomposition during selective laser melting to achieve best ductility in high strength Ti-6Al-4V. Mater Sci Eng A 2018;744:445–55. https://doi.org/10.1016/j.msea.2018.12.047.
[56] Cao S, Chen Z, Lim CVS, Yang K, Jia Q, Jarvis T, Tomus D, Wu X. Defect, microstructure, and mechanical property of Ti-6Al-4V alloy fabricated by high-power selective laser melting. JOM 2017;69(12):2684–92. https://doi.org/10.1007/s11837-017-2581-6.